JGR Space Physics

RESEARCH ARTICLE
10.1029/2021JA029138

Dependence of Parallel Electrical Conductivity in the Topside Ionosphere on Solar and Geomagnetic Activity

F. Giannattasio[1], A. Pignalberi[1], P. De Michelis[1], I. Coco[1], G. Consolini[2], M. Pezzopane[1], and R. Tozzi[1]

[1]Istituto Nazionale di Geofisica e Vulcanologia, Roma, Italy, [2]INAF-Istituto di Astrofisica e Planetologia Spaziali, Roma, Italy

Key Points:

- Analysis of the parallel electrical conductivity in the topside ionosphere by using 6 years of in-situ Swarm A measurements is performed
- The dependence of the parallel electrical conductivity on both solar and geomagnetic activity is investigated
- The comparison with the IRI model allowed estimating the contribution to the parallel conductivity mainly due to particle precipitations

Correspondence to:
F. Giannattasio,
fabio.giannattasio@ingv.it

Citation:
Giannattasio, F., Pignalberi, A., De Michelis, P., Coco, I., Consolini, G., Pezzopane, M., & Tozzi, R. (2021). Dependence of parallel electrical conductivity in the topside ionosphere on solar and geomagnetic activity. *Journal of Geophysical Research: Space Physics*, *126*, e2021JA029138. https://doi.org/10.1029/2021JA029138

Received 15 JAN 2021
Accepted 17 MAY 2021

Abstract The spatial and temporal dynamics of ionospheric currents are among the most evident manifestations of the interaction between the magnetized plasma of solar origin and the magnetosphere-ionosphere system. In this context, a special role is played by field-aligned currents (FACs), which drive energy and momentum exchanges between the magnetosphere and the ionosphere, deeply affecting the energy balance of the latter. One of the most relevant physical quantities that may help to fully characterize FACs is the ionospheric electrical conductivity. Understanding the features associated with this quantity may contribute to the advancement of knowledge on the mechanisms of solar wind-magnetosphere-ionosphere interaction as well as energy storage and dissipation involved in the space weather phenomena. By extending a previous study, we investigate the dependence of the electrical conductivity parallel to the geomagnetic field on solar and geomagnetic activity. To this aim, we considered a six-year long data set of in-situ electron density and temperature values recorded by the Langmuir probes on board the Swarm satellites in the topside ionosphere. With this large data set, we computed global maps of the parallel electron conductivity under both quiet and disturbed conditions, and for different solar activity levels. In both cases, the International Reference Ionosphere (IRI) model allowed estimating the contribution of particle precipitation to electrical conductivity.

1. Introduction

The increasing amount of in-situ measurements available in the topside ionosphere may help to improve our knowledge of the physical processes occurring in the near-Earth environment, their impact in response to forcing from plasma of solar origin, and eventually elaborate mitigation strategies aimed at safely managing space and ground infrastructures (Moldwin, 2008). Among these processes, the amplification and dissipation of high-latitude current systems taking place in the ionosphere play a crucial role in the magnetosphere-ionosphere coupling and may drive several phenomena relevant to space weather (Boteler & Pirjola, 2017; Boteler et al., 1998; Liu & Lühr, 2005; Pirjola et al., 2005; Poedjono et al., 2013). These current systems comprise both the horizontal (Hall and Pedersen) currents flowing in the ionospheric E layer between ∼90 and ∼110 km of altitude (Amm, 1997; Kamide & Baumjohann, 1993), and the field-aligned currents (FACs) linking the solar wind-magnetosphere system with the ionosphere (Zmuda et al., 1966).

From the observational point of view, three main features characterize the spatial distribution of ionospheric currents at high latitudes (Boström, 1964; Iijima & Potemra, 1978; Zmuda & Armstrong, 1974): (i) a more poleward sheet of current flowing toward the magnetosphere in the evening sector and toward the ionosphere in the morning sector, i.e., called Region 1 (R1); (ii) a more equatorward sheet of current flowing toward the ionosphere in the evening sector and toward the magnetosphere in the morning sector, i.e., called Region 2 (R2); (iii) the onset of current flows connecting the regions R1 and R2. Specifically, FACs flowing in opposite directions are connected through electrojets flowing along the auroral oval in the night sector, and through Pedersen currents flowing across the auroral oval. Among these three features, only the first two are relevant for the ionospheric F layer when considering the energy budget of the ionosphere due to the coupling with the magnetosphere. In fact, Hall and Pedersen currents are confined in a thin layer of the ionosphere, peaking between 90 and 110 km of altitude, and their intensity rapidly decreases with height becoming negligible above 200 km of altitude (Brekke & Hall, 1988; de la Beaujardiere et al., 1991; Moen & Brekke, 1993; Rasmussen et al., 1988). For this reason, only the contribution from FACs should

be considered in the topside ionosphere when dealing with ionospheric current systems arising from the magnetosphere-ionosphere coupling.

From the physical point of view, a complete characterization of FACs in the ionospheric F layer requires knowledge of the electrical conductivity in the direction parallel to the main geomagnetic field. The reasons are manifold: (i) electrical conductivity is the physical quantity fundamental to quantify the capability of the ionospheric medium to conduct currents; (ii) Ohm's law relates the current density flowing in a resistive medium to the electric field needed to separate charges via electrical conductivity; and (iii) due to Joule heating, the local energy dissipation of currents in a resistive medium depends on the current density and is inversely proportional to electrical conductivity. Thus, the investigation of electrical conductivity allows us, on one side, to gain information on the currents' features, magnitude, and gradients; and, on the other side, to investigate the magnetosphere-ionosphere energy exchange and dissipation in the ionosphere.

Several studies in the literature approached the characterization of electrical conductivity and/or the estimation of the strength and the spatial distribution of equivalent currents systems in the high-latitude ionosphere by taking advantage of both models and observations (Amm et al., 2015; Föpl et al., 1968; Fuller-Rowell & Evans, 1987; Germany et al., 1994; Holzworth et al., 1985; Kamide et al., 1981; Kirkwood et al., 1988; Marklund et al., 1982; Mende et al., 1984; Moen & Brekke, 1993; Mozer & Serlin, 1969; Pulkkinen et al., 2003; Robinson, Tsunoda et al., 1985; Robinson, Vondrak et al., 1985; Spiro et al., 1982; Takeda, 2002; Takeda & Araki, 1985; Weygand et al., 2011). Although the results achieved were promising, they suffered from the following limitations: (i) theoretical models of electrical conductivity strictly depend on the model used; (ii) empirical models derived from satellite measurements, even though they consider a dependence on latitude, local time, and geomagnetic activity, were not able to capture the small-scale spatial and temporal variations typical, for example, of substorms; (iii) incoherent scatter radar, rocket, ionosonde, balloon, and satellite measurements suffered from low spatial and temporal resolution that prevents the characterization of the fast dynamics and fine structure of the ionosphere. Moreover, almost all the works mentioned were targeted at the ionospheric E layer; similar studies focusing on the ionospheric F layer are poorly represented due to the reduced availability of measurements in this region. Amm et al. (2015), for example, took advantage of electric and magnetic in-situ measurements from the Swarm mission (Friis-Christensen et al., 2006) flying in the F layer at ∼500 km of altitude to retrieve field-aligned, Hall, and Pedersen conductivity at ∼110 km of altitude. In a recent work, Giannattasio et al. (2021), hereafter Paper I, for the first time provided high-resolution maps of electrical conductivity in the direction parallel to the main geomagnetic field in the ionospheric F layer by using in-situ Swarm measurements. Compared to the work by Amm et al. (2015), we used only actual data measured by Langmuir probes to provide climatological maps at the flight altitude of Swarm A, without relying on models to extrapolate the behavior of the conductivity in the E layer. In particular, we provided climatological maps based on 4 years of observations of electron density and temperature at 1 Hz, studied the variation of conductivity with magnetic latitude, magnetic local time, and local season to point out its dependence on the different sunlit conditions, highlighted the North-South hemispheric asymmetry in the electrical conductivity, and estimated the contribution to parallel electrical conductivity mainly due to particle precipitation by subtraction of modeled values obtained through the International Reference Ionosphere (Bilitza, 2018; Bilitza et al., 2017, IRI) empirical climatological model.

In this work, we further extend the study performed in Paper I and focus on the dependence of the electrical conductivity on both solar and geomagnetic activity. Following the same approach applied in Paper I, we show, for the first time, maps of parallel electrical conductivity in the ionospheric F layer under different solar and geomagnetic activity levels in Quasi-Dipole (QD) magnetic coordinates. Finally, by taking advantage of cospatial and simultaneous values of electron density and temperature modeled by IRI at the altitude of the Swarm A satellite, we estimate the contribution to parallel electrical conductivity mainly due to particle precipitation.

The paper is organized as follows: Section 2 is devoted to the description of the data set and the methods used to retrieve the maps; Section 3 shows and then discusses the results obtained in light of the existing literature; while in Section 4 we summarize the main points of this work and drive to conclusions.

2. Data and Methods

2.1. Swarm Observations and Preliminary Analysis

To perform the analysis shown in this work, we used 6 years of Langmuir probes level 1b data recorded at 1 Hz by the Electric Field Instrument (Knudsen et al., 2017) on board the European Space Agency (ESA) Swarm A satellite (Friis-Christensen et al., 2006) from April 1, 2014 to March 31, 2020. During this period the satellite traveled in a nearly circular and polar orbit with an inclination of ∼87.4° at an average altitude of ∼460 km. Swarm A satellite takes about 133 days to cover all the 24 local time hours of the day. Level 1b data were downloaded from the LATEST_BASELINES folder of the ESA dissemination server (ftp://swarm-diss.eo.esa.int). Specifically, 1 Hz Langmuir probes data are those identified by the label "EFIxLPI" and are obtained from 2 Hz data (which are identified by the label "EFIx_LP") by interpolation at full UTC seconds (https://earth.esa.int/eogateway/documents/20142/37627/swarm-level-1b-processor-algorithms.pdf/e0606842-41ca-fa48-0a40-05a0d4824501?version=1.0). They provided: UTC time, the position of the satellite in Earth-centered geographic coordinates (North-East-Center, namely NEC), and in-situ electron density and temperature. The latter were filtered out on the basis of the quality flags provided by the mission team. In particular, we selected electron density and temperature data flagged with Flag_LP = 1 and Flags_T_e or Flags_N_e parameters either equal to 10 or 20. This allowed considering high gain data from the Langmuir probes (https://earth.esa.int/documents/10174/1514862/Swarm_L1b_Product_Definition). Data missed or discarded after the quality flags check were replaced by NaN values in order to guarantee the continuity of the time series.

We used the nonorthogonal QD system of magnetic coordinates (Emmert et al., 2010; Laundal & Richmond, 2017; Richmond, 1995). In detail, in order to pass from NEC to QD coordinates (magnetic latitude and longitude) we first transformed NEC and satellite altitude to geodetic coordinates, then we moved from geodetic to QD coordinates (Emmert et al., 2010). Moreover, the position of the Sun was accounted for by using Magnetic Local Time (MLT) instead of UTC time. This allowed us to organize the data set in bins of magnetic latitude (QD latitude) versus MLT.

2.2. The Computation of Parallel Electrical Conductivity

In order to compute the parallel electrical conductivity at Swarm altitudes, the first hypothesis is that the ion species consist mostly of O^+ with the corresponding density similar to that of electrons, namely $n_i \sim n_e$, such to preserve the quasi-neutrality of ionospheric plasma (Ratcliffe, 1973; Rishbeth & Garriott, 1969).

The second hypothesis is that at Swarm altitudes the contribution of conductivity perpendicular to the main field is negligible; then, only the computation of parallel conductivity really matters (Moen & Brekke, 1990, 1993; H. Wang et al., 2005). This quantity is defined as (Kelley, 2009)

$$\sigma_{\parallel} = n_e e^2 \left(\frac{1}{m_e \nu_e} + \frac{1}{m_i \nu_i} \right), \tag{1}$$

where e is the electron charge, m_e and m_i are the electron and ion masses, respectively, $\nu_e = \nu_{en} + \nu_{ei}$ and $\nu_i = \nu_{in} + \nu_{ie}$ are the collision frequencies of electrons and ions, respectively (the subscripts refer to the species colliding, i.e., electrons, neutrals, and ions). Since $m_e \ll m_i$, in Equation 1 only the first term in parenthesis can be considered, so that we obtain (Cravens, 1997; Rishbeth, 1997)

$$\sigma_{\parallel} = n_e e^2 \frac{1}{m_e \nu_e}. \tag{2}$$

The third hypothesis is that at Swarm altitudes, especially at middle and high latitudes, the electron-ion Coulomb collisions dominate over the elastic collisions with neutrals; as a consequence, ν_{en} is negligible and $\nu_e \simeq \nu_{ei}$ (Aggarwal et al., 1979; Kelley, 2009; Nicolet, 1953; Nishino et al., 1998; Singh, 1966; Takeda & Araki, 1985; Vickrey et al., 1981). The electron-ion collision frequency can be written as (Kelley, 2009)

$$\nu_{ei} = n_e T_e^{-3/2}\left[34 + 4.18 ln\left(\frac{T_e^3}{n_e}\right)\right], \quad (3)$$

where n_e and T_e are the electron density and temperature, respectively. Putting together Equations 2 and 3 we find for the parallel electrical conductivity at Swarm altitude

$$\sigma_\parallel = \frac{e^2 T_e^{3/2}}{\left[34 + 4.18 ln\left(\frac{T_e^3}{n_e}\right)\right] m_e}. \quad (4)$$

According to this equation, there is a strong dependence of $\sigma_\parallel$ on the electron temperature that well underlines the strong connection between conductivity and the energy balance in the ionospheric F layer (Singh, 1966). Moreover, $\sigma_\parallel$ depends only on n_e and T_e (apart from a few constants) that are measured by the Langmuir probes on board the Swarm mission. Thus, we can reliably obtain $\sigma_\parallel$ at Swarm altitude by using Equation 4. Since Swarm measurements of n_e and T_e are in cm^{-3} and K units, respectively, we consistently adopted cgs units, according to which $\sigma_\parallel$ is in (s^{-1}) units. The time series of the computed $\sigma_\parallel$ was mapped into grids binned at $1° \times 1°$ in QD latitude versus MLT coordinates, by considering that 1° longitude corresponds to 4 min in MLT. The values of $\sigma_\parallel$ collected within each bin were filtered out by using a median filter and the median of the filtered set was considered to be representative for each bin. This allowed removing local spikes and highlighting the main climatological features. Errors in $\sigma_\parallel$ were computed by a bootstrap method according to the following steps: (i) 1,000 different subsets sized at 60% of the total number of $\sigma_\parallel$ values falling within each bin were randomly extracted; (ii) the median value of each subset was computed; (iii) the standard deviation of the 1,000 median values computed in step (ii) was assumed as the error associated to $\sigma_\parallel$.

3. Results and Discussion

3.1. Climatological Behavior of the Parallel Electrical Conductivity

The top row of Figure 1 shows climatological maps (i.e., obtained by considering the whole 6-year data set at 1 Hz) of $\sigma_\parallel$ for both the Northern (on the left) and Southern (on the right) hemispheres saturated below 2.5×10^{11} s^{-1} and above 5.0×10^{11} s^{-1}. The minimum and maximum values of $\sigma_\parallel$ are $\simeq$2.0 and $\simeq 6.0 \times 10^{11}$ s^{-1}, respectively. The maximum error, which was computed with the bootstrap method described in Section 2.2, is ~0.7%. The middle row of Figure 1 shows the North-South hemispheric asymmetry computed as: (i) the difference between conductivity in the Northern and Southern hemispheres, respectively, namely $\Delta\sigma_\parallel = \sigma_{\parallel,N} - \sigma_{\parallel,S}$ (on the left) saturated below -1×10^{11} s^{-1} and above 1×10^{11} s^{-1}; (ii) the ratio of the two, namely $\sigma_{\parallel,N}/\sigma_{\parallel,S}$ (on the right) saturated below 0.5 and above 1.5. The bottom row of Figure 1 shows $\sigma_\parallel$ as a function of the QD latitude for fixed MLTs (corresponding to different colors). These curves are the result of a smoothing of the original values performed by using a fourth-order Savitzky-Golay low-pass filter with a smoothing window sized at 17 data points (Savitzky & Golay, 1964), corresponding to 17 s in our time series at 1 Hz.

The features emerging from Figure 1 confirm the results described in Paper I (Figure 2), where we performed the same analysis but using a data set covering a shorter time period (4 years instead of six) of observations. The comparison with that work is straightforward, as we used the same color code and saturation levels for the representation of results. So, to avoid repetition the main features emerging from the climatological study will be only briefly itemized here:

(1) As we can clearly see from both the top and bottom rows of Figure 1, remarkable peaks of $\sigma_\parallel$ occur at different locations. For example, a group of peaks is observed at about ±80° QD latitude and MLT between 09:00 and 12:00, i.e., at magnetic coordinates typical of the polar magnetic cusp (Milan et al., 2017), where electron precipitation brings energy from the dayside open magnetosphere (Brinton et al., 1978; Foster, 1983; Prölss, 2006b); a peak between 0° and ~10° QD latitude and around 06:00 MLT corresponds with the absolute maximum and is associated with the morning overshoot (Stolle

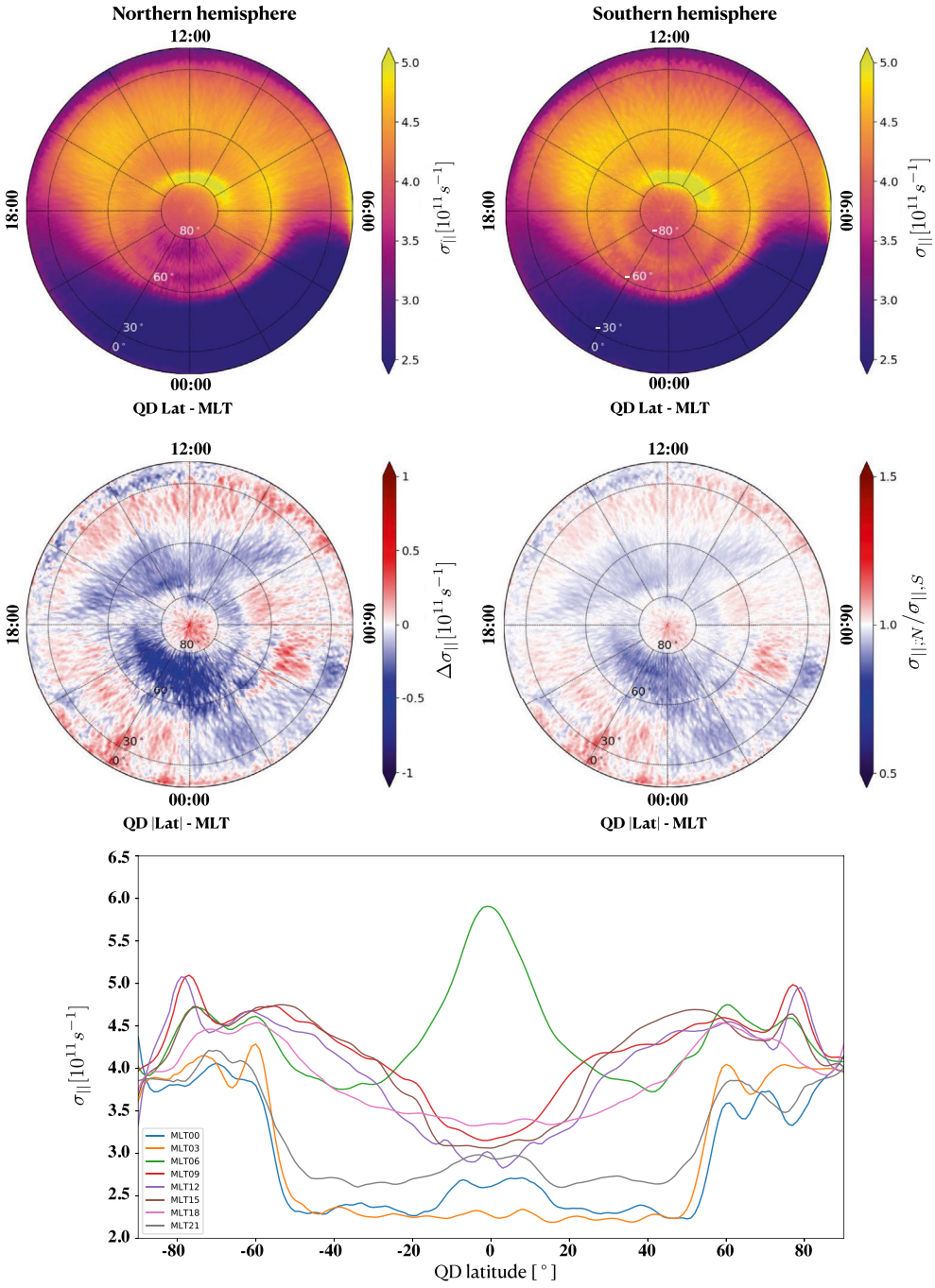

Figure 1. *Top row*: Climatological maps of $\sigma_{\parallel}$ in the Northern (on the left) and Southern (on the right) hemispheres obtained by considering 6 years of Swarm data. The values of $\sigma_{\parallel}$ are saturated below 2.5×10^{11} s^{-1} and above 5.0×10^{11} s^{-1}. *Middle row*: Hemispheric asymmetry of $\sigma_{\parallel}$ computed as both the difference (saturated below -1×10^{11} s^{-1} and above 1×10^{11} s^{-1}, on the left) and the ratio (saturated below 0.5 and above 1.5, on the right) between values in the Northern and Southern hemispheres, respectively. *Bottom row*: $\sigma_{\parallel}$ versus QD latitude for different MLTs (corresponding to different colors) after smoothing with a Savitzky-Golay filter. QD, Quasi-Dipole; MLTs, Magnetic Local Times.

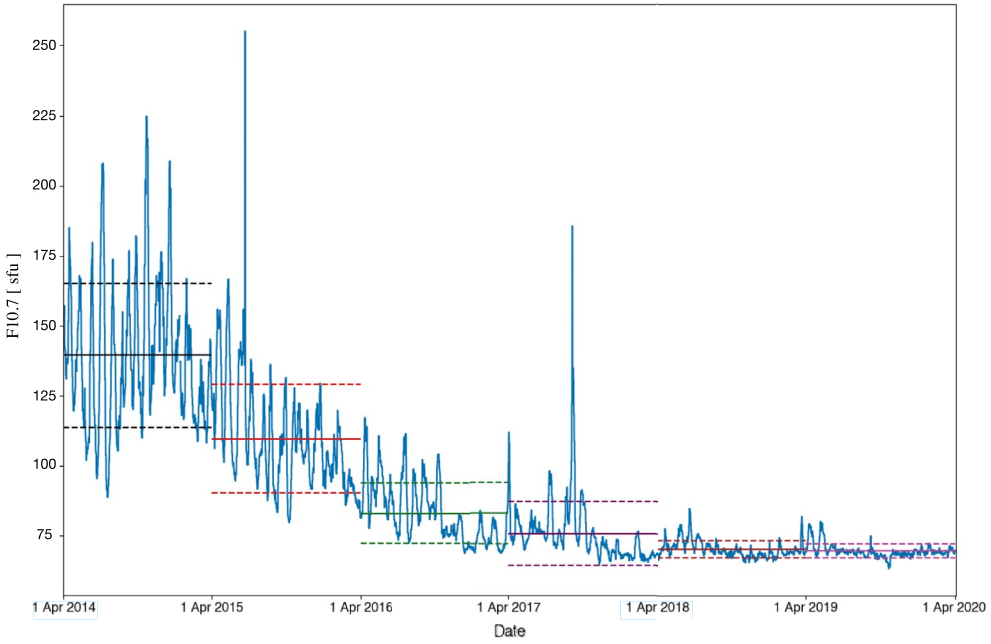

Figure 2. Solar flux at 10.7 cm (blue line) measured during the 6 years of Swarm observations considered in the present study. The horizontal lines in the plot correspond with the yearly mean (the continuous lines) ± one standard deviation (the dashed lines) of the solar flux. Each year is marked by a different color.

et al., 2011), reflecting the steep electron temperature gradient when passing from night to day. Conversely, the lowest values of $\sigma_{\parallel}$ are observed between 21:00 and 03:00 MLT at low QD latitudes. The absolute minimum occurs between 15° and 20° at around 03:00 MLT.

(2) There is an enhancement of $\sigma_{\parallel}$ in the nightside sector between 60° and 70° of QD latitude, where regions R1 and R2 are located (Boström, 1964; Iijima & Potemra, 1978; Zmuda & Armstrong, 1974). In these regions, particle precipitation is the main driver of energy injection, while the effect of extreme ultraviolet (EUV) photoionization is absent.

(3) There is a marked decrease of $\sigma_{\parallel}$ at the dayside dip equator that could be associated with the equatorial ionization anomaly (EIA). It consists of a plasma depletion at the magnetic equator due to the $\mathbf{E} \times \mathbf{B}$ drift that uplifts plasma, which then diffuses poleward along the geomagnetic field lines (Appleton, 1946; Duncan, 1960; Mitra, 1946).

(4) There is a day-night asymmetry in the values of $\sigma_{\parallel}$, for which the dayside conductivity is up to two (or even three) times that on the nightside. This is mainly due to the additional contribution of photoionization by solar EUV radiation on the dayside that is drastically reduced on the nightside.

(5) As visible in the middle row of Figure 1, there is a hemispheric asymmetry for which $\sigma_{\parallel,N} > \sigma_{\parallel,S}$ between 30° and 60° of QD latitude and at all MLTs except for the time range 00:00–04:00 MLT, where $\sigma_{\parallel,N} < \sigma_{\parallel,S}$. Between 60° and 80° of QD Latitude $\sigma_{\parallel,N} < \sigma_{\parallel,S}$ at all MLTs, especially between 20:00 and 02:00 MLT, where $\sigma_{\parallel,N}/\sigma_{\parallel,S} \simeq 0.75$. Above 80° of QD Latitude, in the polar cap, $\sigma_{\parallel,N} > \sigma_{\parallel,S}$. The asymmetry is probably due to the different sunlit conditions of both hemispheres and to seasonal effects (Cnossen & Förster, 2016; Giannattasio et al., 2021). Note that slight hemispheric asymmetries (up to a few hundred Kelvin) are also present in the IRI model of T_e at high latitudes (Lomidze et al., 2018).

3.2. Variation of Parallel Electrical Conductivity With Solar Activity

The level of solar activity during the 6 years of Swarm observations considered in the present study was evaluated by using the daily solar flux at 10.7 cm (F10.7) as a proxy. The time series containing F10.7 was downloaded from the Space Physics Data Facility of the NASA Goddard Space Flight Center (OMNI data set, https://cdaweb.gsfc.nasa.gov/). Figure 2 shows F10.7 (blue line) measured from April 1, 2014 to March 31, 2020 in units of J s^{-1} m^{-2} Hz^{-1} (also known as solar flux units, sfu). Each year (from 1 to 6) is marked

Table 1
Year-by-Year Mean and Standard Deviation of the Solar Flux at 10.7 cm (F10.7) in Units of 10^{-22} J s^{-1} m^{-2} Hz^{-1} (Solar Flux Units, sfu) During the Period of Swarm Observations, From April 1, 2014 to March 31, 2020

Year[a]	Mean F10.7 (sfu)	Std. Dev. F10.7 (sfu)	Minimum $\sigma_{\parallel}$ (10^{11} s^{-1})	Maximum $\sigma_{\parallel}$ (10^{11} s^{-1})	Maximum error (%)
1	141.72	51.77	0.9	5.0	2.2
2	109.76	19.29	0.8	4.6	1.6
3	83.15	10.90	0.7	4.6	1.9
4	75.81	11.41	0.6	4.6	2.2
5	70.22	3.04	0.6	4.5	3.6
6	69.65	2.45	0.6	4.4	3.6

Note. For each year, corresponding minimum and maximum values of $\sigma_{\parallel}$, along with the maximum associated error, are also shown.
[a]Since April 1, 2014.

by a different color. The horizontal lines in the plot correspond with the yearly mean (the continuous lines) ± one standard deviation (the dashed lines) of the solar flux. These values are listed in the second and third columns of Table 1 and together with Figure 2 clearly show, as it is well known, that solar activity during the 6 years of Swarm observations decreased to its minimum. In particular, the yearly mean value of F10.7, which gives information on the solar energy that reached the top of the Earth's atmosphere, decreased from almost 142 to almost 70 sfu. Accordingly, the yearly standard deviation of F10.7, which gives information on how much values are dispersed with respect to the mean, decreased as well. Of course, the shape of F10.7 does not make the mean and standard deviation effective estimators, but nonetheless they represent coarse indicators of the solar energy variations to which the Earth's atmosphere is subjected. Thus, investigating the yearly changes of $\sigma_{\parallel}$ offered the possibility to point out its dependence on solar activity. Moreover, it represents an excellent compromise: on the one hand 1 year of observations at 1 Hz provides a statistics that is robust enough to reliably estimate $\sigma_{\parallel}$ in both hemispheres, at all QD latitudes, and at all MLTs; on the other hand, selecting 1 year at a time includes the possibility to weigh the seasons almost the same for each year. Thus, although seasonal effects play an important role on the dynamics of the ionospheric F layer including, of course, the features that characterize $\sigma_{\parallel}$ (Paper I), they affect the same each selected year. This is also in accordance with previous literature. For example, Medvedeva and Ratovsky (2019) demonstrated that the average of the F2-peak electron density (*Nm*F2) well correlates with F10.7. This ensures that the seasonal dependence of $\sigma_{\parallel}$ introduces a negligible bias when studying its yearly variation with solar cycle.

Figure 3 shows the yearly variation during the 6 years of Swarm observations used in this work (from left to right) of $\sigma_{\parallel}$ in the Northern and Southern hemispheres (first and second rows, respectively) saturated below 2.5×10^{11} s^{-1} and above 5×10^{11} s^{-1}; the hemispheric asymmetry of $\sigma_{\parallel}$ computed as the difference (third row) and the ratio (fourth row) between values in the Northern and Southern hemispheres, saturated below -1×10^{11} s^{-1} and above 1×10^{11} s^{-1}, and below 0.5 and above 1.5, respectively. The maximum error associated with each yearly data set of $\sigma_{\parallel}$, which was computed with the bootstrap method described in Section 2.2, is reported in the last column of Table 1. The most remarkable features emerging from Figure 3 are:

- Moving from year 1 to year 6, and thus with the decrease of solar activity, both minimum and maximum values of $\sigma_{\parallel}$ decrease, as we reported in the fourth and fifth columns of Table 1. At the same time, when inspecting yearly plots similar to that shown in the bottom row of Figure 1, we notice that the extreme values of $\sigma_{\parallel}$ in each yearly map always occur at the magnetic equator: the maximum being around 06:00 MLT, the minimum in the night hours.
- Moving from year 1 to year 6, $\sigma_{\parallel}$ in the dayside decreases. In more detail, peaks of $\sigma_{\parallel}$ that are present in the dayside of year 1, especially in the Southern hemisphere at QD latitudes between 30° and 60°, become weaker and weaker with time. $\sigma_{\parallel}$ in the dayside is up to three times higher than in the nightside in years 1 and 2. This day-night asymmetry reduces to up to two times in year 6.

The features between about 04:00 and 20:00 MLT at QD latitudes typically associated with the cusp become smaller and fainter from year 1 to year 6. Moreover, their extension in MLT progressively decreases. Also $\sigma_{\parallel}$ at 06:00 MLT, in correspondence with the morning overshoot, tends to be fainter with the decrease of solar activity

- The features of $\sigma_{\parallel}$ on the nightside at auroral QD latitudes tend to enhance with the decrease of solar activity. For example, $\sigma_{\parallel}$ at QD latitudes $\gtrsim$60° on the nightside during years 5 and 6 tends to be comparable or even higher than that in the cusp regions.
- During year 1, when the solar activity is the highest, $\sigma_{\parallel}$ is substantially higher (from one to two times in the Southern hemisphere than in the Northern hemisphere at almost all QD latitudes and MLTs, except at very high QD latitudes and, in small patches, at low latitudes on the nightside. Then, starting from

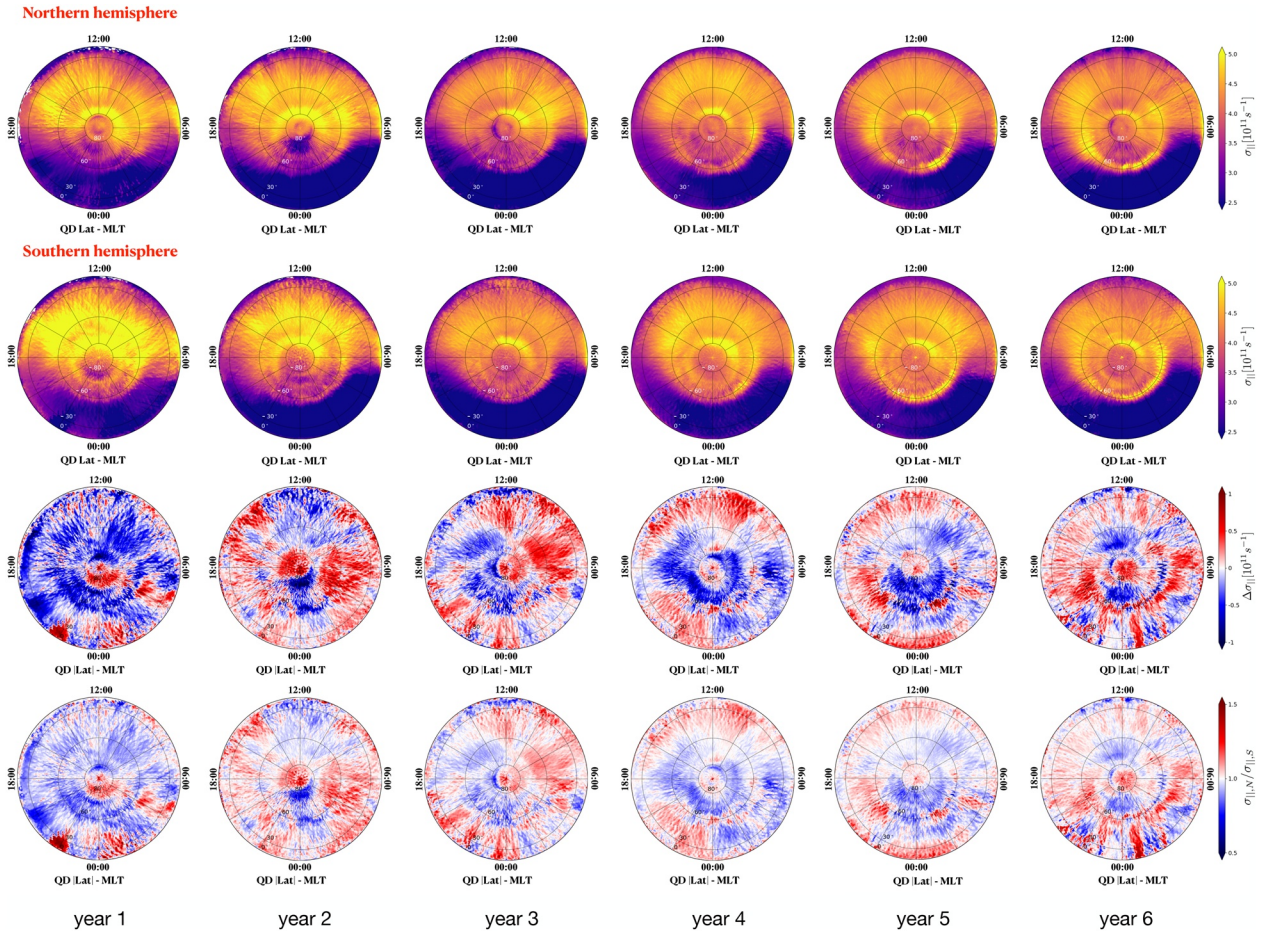

Figure 3. *From left to right*: Yearly variation of $\sigma_{\parallel}$ maps from year 1 to year 6 (see also Figure 2). *From top to bottom*: (1) Maps of $\sigma_{\parallel}$ in the Northern hemisphere saturated below 2.5×10^{11} s^{-1} and above 5×10^{11} s^{-1}; (2) maps of $\sigma_{\parallel}$ in the Southern hemisphere saturated below 2.5×10^{11} s^{-1} and above 5×10^{11} s^{-1}; (3) hemispheric asymmetry of $\sigma_{\parallel}$ computed as the difference between values in the Northern and Southern hemispheres, respectively, and saturated below -1×10^{11} s^{-1} and above 1×10^{11} s^{-1}; (4) hemispheric asymmetry of $\sigma_{\parallel}$ computed as the ratio between values in the Northern and Southern hemispheres, respectively, and saturated below 0.5 and above 1.5.

year 2, the asymmetry patterns change completely and in a complicated way, such that it is not trivial to derive a clear behavior.

The results found are consistent with the previous literature and are mainly due to the influence of solar activity on both n_e and T_e, which are the only contributors to $\sigma_{\parallel}$ in the ionospheric F layer. In particular, while n_e always increases with solar flux, the behavior of T_e is much more complicated and crucially depends on the altitude, local time and season (Bilitza et al., 2007). Despite this, the increase of $\sigma_{\parallel}$ on the dayside at all QD latitudes with solar activity was agreed to be mainly due to electron temperature variation (which dominates in the computation of $\sigma_{\parallel}$) with changing EUV emissions from the Sun, although a minor contribution may come directly from n_e. For example, since early works on this topic, T_e was found to increase with solar emissions at a rate of a few degrees K per sfu (Willmore, 1965). Sharma et al. (2004) found that T_e enhances during solar flares on the dayside. Their estimated enhancement for the average T_e is from 1.3 to 1.9 times with respect to the average value during normal days and crucially depends on local time. On the contrary, solar flares do not significantly affect the nightside ionosphere, at least in the altitude range between 425 and 625 km. Chamua et al. (2007) found that T_e on both the dayside and the nightside holds a positive correlation with solar activity when averaged on shorter (monthly) time scales. However, on a longer (yearly) time scale, the correlation exhibits a time lag of about 1 year, suggesting a sort of inertia to variations in solar flux leading to a nonlinear variation of ionospheric parameters with solar flux.

If, on one side, the increase in solar activity provides an increased production in photoelectrons and, consequently, of the electron heating rates and electron temperature, on the other side the ion concentration also increases. This gives rise to an increased collisional cooling rate (due to electron-ion collisions) and a following decrease of T_e (Schunk & Nagy, 1978). Thus, the resulting pattern of T_e, and consequently, of $\sigma_\parallel$, should be a net balance between the two.

The positive correlation between solar activity and the values of $\sigma_\parallel$ in correspondence with the morning overshoot is apparently in contrast with the results shown by Stolle et al. (2011). In fact, they reported an anticorrelation between T_e, on which $\sigma_\parallel$ mainly depends, and the solar flux due to the dominance of electron cooling deriving from electron-ion collisions with respect to the thermal heating deriving from the increase in solar EUV. However, in that work the values of T_e were based on 8 years of CHAMP observations (Reigber et al., 2002), during which the satellite flew at altitudes from ∼410 km down to ∼310 km. Moreover, taking also advantage of both models and radar observations, the authors argued that a positive correlation between T_e and the solar flux should be instead observed at altitudes higher than ∼400 km. This means that like n_e, T_e also shows a positive correlation with F10.7 at Swarm altitudes, which justifies the observed behavior of $\sigma_\parallel$ at all MLTs and QD latitudes.

Particularly interesting is the enhancement of $\sigma_\parallel$ with the decrease of solar activity in the nightside at QD latitudes around 60° in both hemispheres. This is a nontrivial result. In fact, although it is known that particle precipitation on the nightside (associated with substorms, dynamic processes occurring in the geomagnetic tail, and the coupling with the plasmasphere) play a fundamental role in exchanging heat with the ionosphere from subauroral latitudes upwards (Brace et al., 1982; Gololobov & Golikov, 2019; Kofman & Wickwar, 1984; Prölss, 2006b), it remains to be understood why there is an amplification of these effects when solar activity decreases, as it is evident from Figure 3. Even more so because at solar minimum T_e on the nightside is expected to respond significantly less to variations of the geomagnetic activity level (Brace, 1990). Prölss (2006b) studied the enhancement of T_e on the nightside using satellite data and found that the enhanced T_e region spatially coincides with the position of the main ionospheric trough. A possible explanation could be that on the nightside, during periods of low solar activity, the contribution to T_e from the collisional cooling should collapse, due to the simultaneous collapse of both the electron and ion density in the ionospheric F layer. Therefore, in the absence of effects that counterbalance that of the precipitating particles (which also occurs even in conditions of solar quietness), the net T_e can increase due, e.g., to energy exchanges with the nightside magnetosphere. This is consistent with the scenario according to which T_e is significantly enhanced in regions of depleted n_e, while, on the contrary, it significantly decreases in regions of enhanced n_e as a result of enhanced energy loss to the ions (Wang et al., 2006).

3.3. Variation of Parallel Electrical Conductivity With Geomagnetic Activity According to the AE Index

The level of geomagnetic activity during almost 4 of the 6 years of Swarm observations considered in the present study was evaluated by using the well-known one-minute Auroral Electrojet index (AE) as a proxy (Davis & Sugiura, 1966). The time series of AE, which is derived from variations in the horizontal component of the geomagnetic field observed at 12 selected observatories along the auroral zone in the Northern hemisphere, was downloaded from the Kyoto World Data Center (http://wdc.kugi.kyoto-u.ac.jp/aedir/). However, the data center ceased to provide AE data after February 28, 2018. For this reason, our AE time series ranges between April 1, 2014 and February 28, 2018. One question may arise: Why don't you use as a proxy of the geomagnetic activity level another high-latitude and high-resolution index like the SME index (the equivalent to AE) currently available from the SuperMAG initiative (Gjerloev, 2009). This would provide two main advantages: (1) SME is computed by considering data from about 100 observatories in the Northern hemisphere at latitudes above ∼55°. (2) Uninterrupted SME data are available from mid-1975 to December 31, 2019. However, we should also consider that: (1) Despite SME was proved to be a robust index for probing the geomagnetic activity (Newell & Gjerloev, 2011), the spatial coverage of the stations at high latitudes is rather inhomogeneous. (2) Unlike AE, the SME index is (still) not the official standard recognized by the International Association of Geomagnetism and Aeronomy (IAGA). (3) Being based on a different definition respect to AE, the SME index values cannot be immediately compared to the AE values found in the literature and it is not trivial to establish threshold values to select quiet and/or disturbed

events. As we give special emphasis to the middle and high QD latitudes, where parallel conductivity plays a key role in regulating the energy balance of the ionosphere and the coupling with the magnetosphere, we decided to use the standard AE index instead of the SME one, even though the corresponding time series is 22 months shorter.

Figure 4 shows maps of $\sigma_\parallel$ in the Northern and Southern hemispheres (on the left and on the right, respectively) saturated below 2.5×10^{11} s^{-1} and above 5×10^{11} s^{-1} for two different levels of geomagnetic activity: quiet (AE < 50 nT, panel a)) and disturbed (AE > 150 nT, panel b)). In the second row of each panel, we also show the hemispheric asymmetry of $\sigma_\parallel$ computed as the difference (on the left) and the ratio (on the right) between values in the Northern and Southern hemispheres and saturated below -1×10^{11} s^{-1} and above 1×10^{11} s^{-1}, and below 0.5 and above 1.5, respectively. The maximum errors associated with $\sigma_\parallel$ are: 3.1% for the case of quiet geomagnetic activity (AE < 50 nT) and 1.3% for the case of disturbed geomagnetic activity (AE > 150 nT). The most remarkable features emerging from Figure 4 are:

- In the Northern hemisphere, during quiet conditions, peaks of $\sigma_\parallel$ are observed on the dayside at QD latitudes around ∼80°, where the value of $\sigma_\parallel$ saturates. Slightly lower values of $\sigma_\parallel$, between 4.5 and 5.0×10^{11} s^{-1}, are observed at QD latitudes around ∼60° between 06:00 and 08:00 MLT, and at low latitudes around 06:00 MLT (in correspondence with the morning overshoot). On the nightside, $\sigma_\parallel$ is enhanced at high QD latitudes up to $\sim 4.5 \times 10^{11}$ s^{-1} starting from around ∼60° of QD latitude upwards. The same features are also observed in the Southern hemisphere. In both hemispheres, the minimum values of $\sigma_\parallel$ are observed between 00:00 and 03:00 MLT and low QD latitudes.
- During disturbed conditions, the same features as in quiet conditions are observed, but their spatial extent and the associated values of $\sigma_\parallel$ appreciably increase, especially in the Southern hemisphere, where, e.g., features at QD latitudes ∼80° on the dayside are also visible after dusk, and extend to MLTs up to ∼22:00. This is consistent with the work of Prölss (2006a), according to which the characteristic dayside feature associated with the cusp tends to move slightly (about 1° for each increase of AE by 100 nT) equatorward with increasing geomagnetic activity.
- Likewise for the climatological case and the yearly selection case examined in the previous subsections, there is a day-night asymmetry in the values of $\sigma_\parallel$, for which the dayside conductivity is up to two to three times that on the nightside. This is a general characteristic of $\sigma_\parallel$ and is due to the additional action of photoionization by solar EUV radiation on the dayside.
- The hemispheric asymmetry manifests in different ways depending on the geomagnetic activity level. During quiet conditions, at low latitudes $\sigma_{\parallel,N}$ exceeds $\sigma_{\parallel,S}$ at almost all MLTs. On the dayside, this happens at QD latitudes up to ∼60° and even at higher latitudes from 04:00 to 08:00 MLT, on the nightside in the same range of latitudes between 18:00 and 00:00 MLT. On the contrary, $\sigma_{\parallel,S}$ is up to 2 times higher than $\sigma_{\parallel,N}$ at QD latitudes poleward of ∼60° at almost all MLTs, especially between 60° and 80° around midnight.
- During disturbed conditions, hemispheric asymmetries are noticeably different. In fact, the regions where $\sigma_{\parallel,N} < \sigma_{\parallel,S}$ are greatly reduced and occupy mainly the sector between 18:00 and 00:00 at QD latitudes between 60° and 80°. In the polar cap, $\sigma_{\parallel,N} > \sigma_{\parallel,S}$, probably due to direct precipitations during periods when the magnetosphere is in an open configuration. The asymmetry is likely due to the different sunlit conditions of both hemispheres and to seasonal effects (Cnossen & Förster, 2016; Giannattasio et al., 2021). However, a contribution to asymmetry may also arise due to the selection based on the AE index, which is well defined only in the Northern hemisphere.

We checked the presence of seasonal effects in the data and performed a double conditioning on both the AE index and the season. We obtained conductivity maps very similar to those shown in Section 3.2 of Paper I for the case of data selection based on the local season only.

In order to better point out the dependence of $\sigma_\parallel$ on the geomagnetic activity, in the top panels of Figure 5 we show the ratio between $\sigma_\parallel$ computed during periods with AE > 150 nT and the same quantity computed during periods with AE < 50 nT for both the Northern (on the left) and Southern (on the right) hemispheres. As we can see, some interesting features emerge:

- In both hemispheres, $\sigma_\parallel$ clearly increases (up to almost 1.5 times) with the geomagnetic activity in the auroral regions at all MLTs and at QD latitudes typically associated with regions R1 and R2 (Paper I). An intense increase is also observed at subauroral QD latitudes ($\lesssim$60°), especially in the sector between

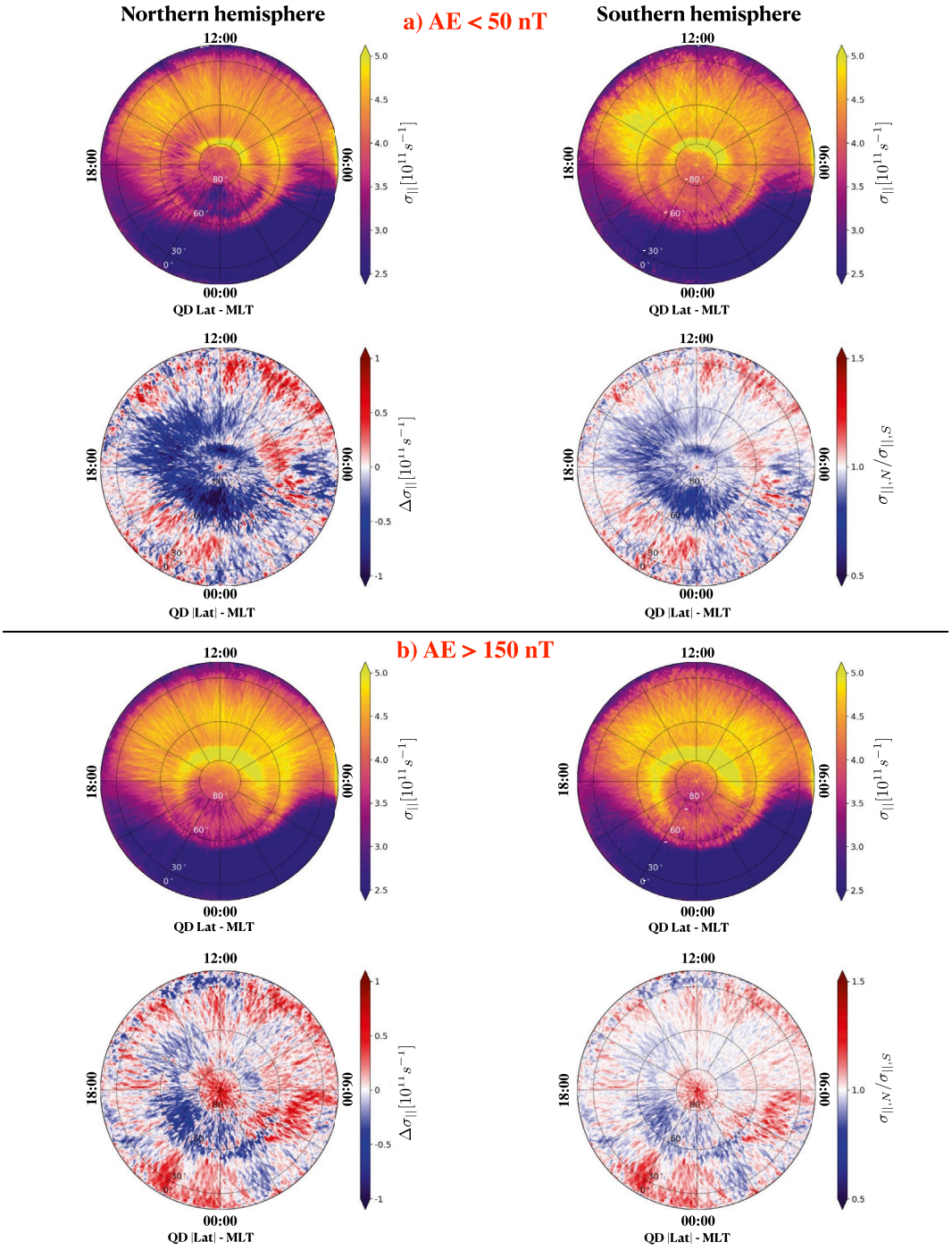

Figure 4. *Panel* (a): Maps of $\sigma_{\parallel}$ in both the Northern (top-left) and Southern (top-right) hemispheres during quiet levels of geomagnetic activity (AE < 50 nT), together with the hemispheric asymmetry of $\sigma_{\parallel}$ computed as both the difference (bottom-left) and the ratio (bottom-right) between values in the Northern and Southern hemispheres, respectively. Value maps are obtained by considering almost 4 years of data, from April 1, 2014 to February 28, 2018, and are saturated below 2.5×10^{11} s^{-1} and above 5.0×10^{11} s^{-1}. Asymmetry maps are saturated below -1×10^{11} s^{-1} and above 1×10^{11} s^{-1} (the difference $\Delta\sigma_{\parallel}$) and 0.5 and 1.5 (the ratio $\sigma_{\parallel,N}/\sigma_{\parallel,S}$), respectively. *Panel* (b): The same as panel (a), but during disturbed levels of geomagnetic activity (AE > 150 nT). AE, Auroral Electrojet.

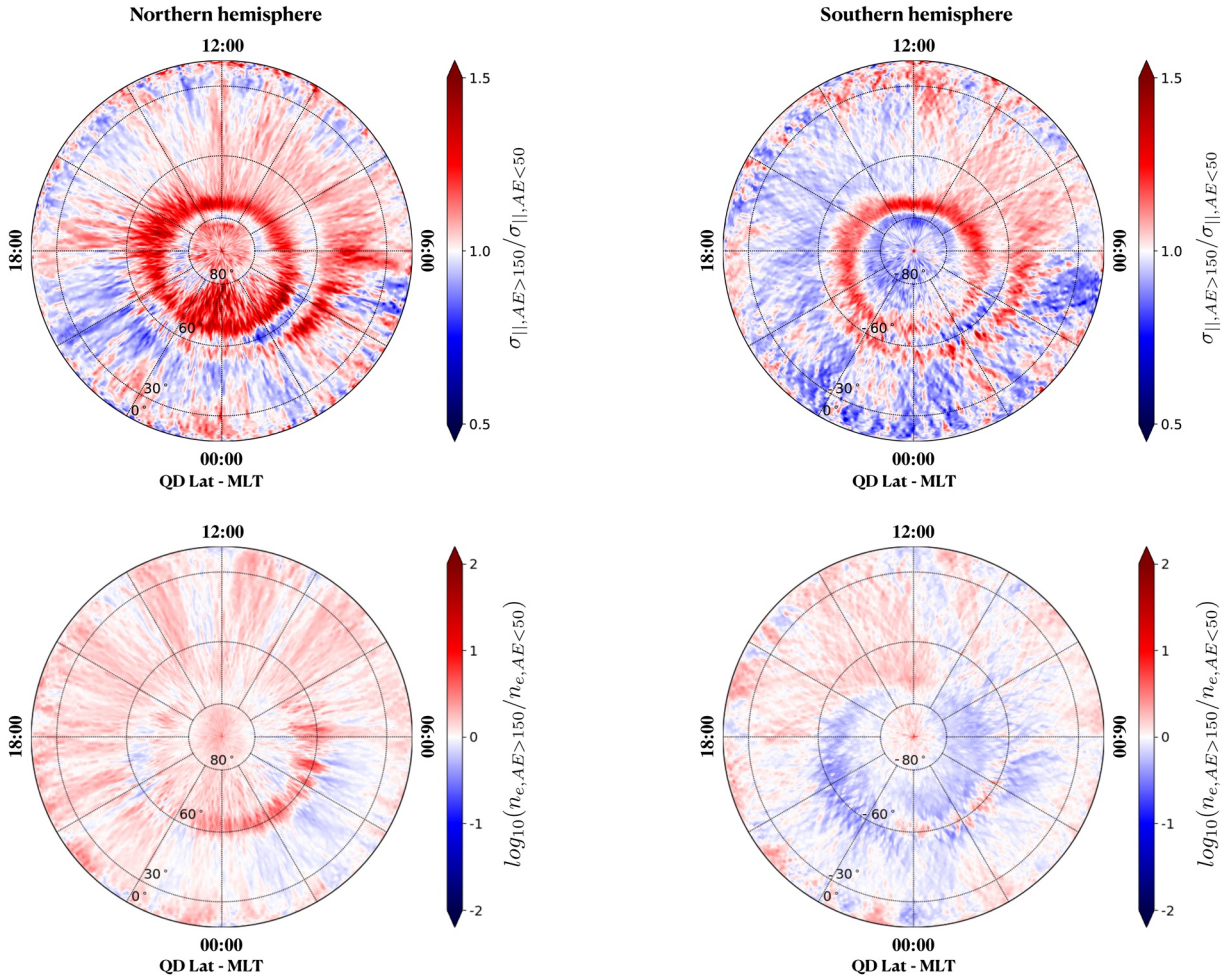

Figure 5. *Top panels*: Ratio between $\sigma_{\parallel}$ during disturbed geomagnetic activity levels (AE > 150 nT) and the same quantity during quiet geomagnetic activity levels (AE < 50 nT) for both the Northern (on the left) and Southern (on the right) hemispheres. *Bottom panels*: Logarithm of the ratio between n_e during disturbed geomagnetic activity levels (AE > 150 nT) and the same quantity during quiet geomagnetic activity levels (AE < 50 nT) for both the Northern (on the left) and Southern (on the right) hemispheres. AE, Auroral Electrojet.

02:00 and 06:00 MLT of the Northern hemisphere. A diffuse increase is present in both hemispheres between 06:00 and 10:00 MLT and above 30° QD latitude, and in the Northern hemisphere also between 10:00 and 12:00 MLT, and 16:00 and 18:00 MLT at the same latitudes.

- Interestingly, $\sigma_{\parallel}$ increases in the polar cap of the Northern hemisphere and decreases in the same region of the Southern hemisphere with geomagnetic activity.
- There are diffuse regions where $\sigma_{\parallel}$ decreases with the geomagnetic activity, especially in the Southern hemisphere (e.g., at mid-QD latitudes and MLT in the range 12:00–06:00).

It is well known that during disturbed geomagnetic periods, both the electron temperature and the density undergo short-term variations due to the transfer of energy and momentum from the magnetosphere to the upper ionosphere, whose response is nonlinear (Afonin et al., 1997; Brace et al., 1988; Brinton et al., 1978; Evans, 1970; Fok et al., 1991; Kozyra et al., 1986; Prölss, 2006b; Rishbeth & Müller-Wodarg, 1999). These variations are reflected in those of $\sigma_{\parallel}$. For example, the enhancement of T_e under disturbed conditions at middle latitudes in the nightside was pointed out in the early works of Evans (1970) based on incoherent scatter radar data, and was followed by studies relying on satellite measurements (Afonin et al., 1997; Brace et al., 1988; Brinton et al., 1978; Fok et al., 1991; Prölss, 2006b). This enhancement is often colocated with the equatorward edge of the trough (Brace et al., 1988; Brinton et al., 1978). A possible explanation for the enhancement of T_e involves the interaction between photoelectrons produced by solar EUV and driven in

the plasmasphere along the geomagnetic field lines, and the ring current (Cole, 1967). According to this scenario, hot electrons heated by Coulomb collision with ring current ions from the plasmasphere may be transported along the geomagnetic field lines down to the ionosphere and heat local thermal electrons, sustaining and enhancing, in this way, T_e in the nightside ionosphere. This should generate an almost permanent feature amplified or not during disturbed or quiet periods.

Also n_e contributes to the variations of T_e and, thus, of $\sigma_\parallel$, mainly in two ways. First, a variation of n_e gives rise to a variation of the thermal electron gas heat capacity (that is proportional to n_e). Second, the increase in n_e corresponds with an increase in collisional cooling due to the increased rate of collision between electrons and ions (McDonald & Williams, 1980). For example, in particular, the latter provides support for both observations and models asserting the anticorrelation between n_e and T_e (Prölss, 2006b; Wang et al., 2006). In the theoretical model presented by Wang et al. (2006), T_e is found to be enhanced by a factor 2 to 4 inside the trough at middle latitudes during disturbed conditions with respect to quiet ones. In this model, the increase of T_e at middle latitudes extends from about 62.5°N around 22:00 LT to about 52.5°N around midnight, then moves back to higher latitudes in the early morning. The shape of this enhancement resembles that of the edge of the middle latitude trough. Thus, the combined action of both the increase of T_e due to hot electrons from the magnetosphere and the decrease of n_e may result in the subauroral features of $\sigma_\parallel$ present in all the figures shown in this paper and particularly in Figure 5, where it is shown that these features are related with the geomagnetic activity.

To better point out the role of n_e and, in particular, of its variation with the geomagnetic activity in the F-layer (nightside) dynamics, in the bottom panels of Figure 5, we show the logarithm of the ratio between n_e during disturbed geomagnetic activity levels (AE > 150 nT) and the same quantity during quiet geomagnetic activity levels (AE < 50 nT) for both the Northern (on the left) and Southern (on the right) hemispheres. In the Northern hemisphere, at QD latitudes between ∼60° and ∼65°, n_e greatly enhances between 22:00 and 06:00 MLT. Such an increase can reach up from 10 to almost 100 times the values of n_e during geomagnetic quiet conditions. In the same sector, at QD latitudes $\lesssim$60°, n_e decreases up to about 10 times with respect to periods of quiet geomagnetic activity. In the remaining latitudes and MLTs in the Northern hemisphere there is an overall enhancement of n_e with geomagnetic activity up to about 3–4 times. In the Southern hemisphere, n_e undergoes a completely different behavior. In the nightside auroral regions, n_e diffusely decreases with geomagnetic activity by a factor $10^{-0.5}$–10^{-1}, except for a thin region centered at 60° QD latitude and between 00:00 and 04:00 MLT. A slight increase in n_e occurs on the dayside between noon and dusk at QD latitudes up to ∼75° at noon and ∼60° at dusk, respectively. In the Southern polar cap, n_e remains almost the same with increasing geomagnetic activity. By comparing top panels with the bottom ones in Figure 5, we observe that the strong enhancements in $\sigma_\parallel$, and consequently in T_e, located inside the auroral regions of the Northern hemisphere correspond with regions of diffuse enhancement of n_e values. Moreover, the equatorward boundary of the auroral enhancement of $\sigma_\parallel$ is colocated with the peak of n_e. This is consistent with the role played by precipitating particles, which are associated with current systems flowing in the ionosphere and from (toward) the magnetosphere within regions R1 and R2 (as pointed out in Paper I), in the simultaneous rising of $\sigma_\parallel$ and n_e with the increasing geomagnetic activity. At QD latitudes immediately lower than ∼60° the increase of $\sigma_\parallel$ in the Northern hemisphere is associated with the decrease in n_e in the same region. This is probably due to the reduced collisional cooling that prevents the decrease of T_e and, thus, of $\sigma_\parallel$. Thus, we are probably observing the region where the transition from R2 to the trough occurs, where both the processes involving particle precipitation to the auroral regions, on one side, and heating favored by electron evacuation at the trough edge, on the other side, are simultaneously present. This is also consistent with the nightside features observed with decreasing solar activity (see Section 3.2 and Figure 3) and provides a plausible interpretation of what found in both Paper I and the present work.

Regarding the lowering of $\sigma_\parallel$ with the increase of geomagnetic activity in the polar cap of the Southern hemisphere, it is not clear what mechanism is causing this different behavior with respect to the Northern hemisphere (where, on the contrary, $\sigma_\parallel$ increases with the geomagnetic activity). In light of the discussion above, this behavior could be ascribed to the electron collisional cooling due to the increase in n_e, but there is no apparent reason why the opposite behavior should occur in the polar cap of the Northern hemisphere. The same reasoning applies to other features like, e.g., the decrease of n_e with geomagnetic activity in the Southern hemisphere at almost all MLTs and QD latitudes between ∼60° and ∼80°. Possibly there are

seasonal effects that are not considered in the selection of the different geomagnetic activity levels based on AE index, and that will be investigated in the future. In fact, seasons are mixed inside quiet and disturbed periods, and the statistical prevalence of some of them may be responsible for the hemispheric asymmetries pointed out here. On the other hand, it is well known that n_e, T_e, and thus $\sigma_\parallel$ have a pronounced dependence on the sunlit conditions (see Paper I and references therein).

3.4. The Contribution of Particle Precipitation and Reduced Cooling

As we pointed out in Paper I (see the corresponding Figure 1), for QD latitudes $\gtrsim$60° and $\lesssim$80° the enhancement of $\sigma_\parallel$ can be associated with the typical patterns of regions R1 and R2. These are clearly visible on the nightside and are mainly due to particle precipitation that injects energy into the auroral regions. Another remarkable increase in $\sigma_\parallel$ is observed in the dayside sector at ∼80° of QD latitude and is associated with the cusp region (Milan et al., 2017), where intense particle precipitations occur from the dayside magnetosphere into the ionosphere (Brinton et al., 1978; Foster, 1983; Prölss, 2006a). However, as discussed in the previous section, particle precipitation is not the only mechanism that contributes to modify $\sigma_\parallel$, particularly on the nightside, where an additional contribution from electron depletion at middle latitudes may occur due to the anticorrelation between n_e and T_e around the trough (Lomidze et al., 2018; Wang et al., 2006). Both contributions are not currently modeled by the IRI model, which became the official International Standardization Organization (ISO) standard for the ionosphere (Bilitza, 2018; Bilitza et al., 2017).

IRI was run to provide n_e and T_e values cospatial and simultaneous with Swarm observations at the same sampling rate. For the topside we used the NeQuick topside option (Coïsson et al., 2009; Nava et al., 2008) which is the default option in IRI and proved to be the best option, especially for disturbed conditions (Pignalberi et al., 2016). Regarding T_e, the model provided by Truhlik et al. (2012) has been used, which also takes into account the variation with solar activity. Like any other empirical model, IRI performances strongly depend on the underlying data sets on which its analytical formulas are based. As a result of the scarcity of both electron density and temperature data for the topside ionosphere and for very high latitudes, the IRI performances in such cases can be lower. Nevertheless, several works demonstrated that IRI, although being an empirical climatological model, is much more reliable than most physics-based models in representing the physical conditions of the ionosphere at high latitudes (Shim et al., 2011, 2012; Tsagouri et al., 2018). Moreover, being meant for a climatological description of the diurnal, seasonal, spatial, solar, and magnetic activity effects on the ionospheric plasma, not all the phenomena affecting it, like, e.g., particle precipitation, are described by the model. However, besides the IRI model, there exist different ionospheric empirical models at a regional scale able to provide even better performances than IRI but for a selected region or latitudinal range. This is, e.g., the case of the E-CHAIM model (Themens et al., 2017) that is confined to the Northern hemisphere high latitudes. Due to the global-scale nature of our investigation and to make consistent the results across the different latitudinal regions, the IRI model resulted the best option. For all the above reasons, it is reasonable to think that the subtraction of $\sigma_\parallel$ computed via Equation 4 with n_e and T_e provided by IRI from the same quantity obtained by Swarm observations, provides an estimate of the contributions to $\sigma_\parallel$ *in primis* due to particle precipitation (Paper I).

Figure 6 shows, from top to bottom, the yearly variation of the quantity $\sigma_{\parallel,Swarm} - \sigma_{\parallel,IRI}$ with the solar activity (as discussed in Section 3.2), i.e., from April 1, 2014 to March 31, 2020 for both the Northern (on the left) and the Southern (on the right) hemispheres. The enhancements in this map point out the contributions to conductivity not modeled by IRI as a function of the solar activity (which decreases from year 1 to year 6, see Figure 2). The most interesting feature emerging is the enhancement of these contributions on the nightside with the decrease of solar activity in both hemispheres. This feature becomes more and more intense (up to saturation) and extended with time, and develops from dusk to dawn around ∼60° of QD latitude. It is probably due to the heating induced by particle precipitation from the magnetosphere to the ionosphere and captures the joint action of precipitation and the electron depletion at the transition between region R1 and the edge of the trough. Other spurious features not properly modeled by IRI are located in the dayside during the highest levels of solar activity (years 1 and 2), especially in the Southern hemisphere at almost all QD latitudes. On the other side, in the Northern hemisphere such contributions are mostly located at low and middle latitudes. Finally, Figure 6 shows that also the position and strength of the morning overshoot are not correctly modeled by IRI, and its associated features increase with the decrease of solar activity.

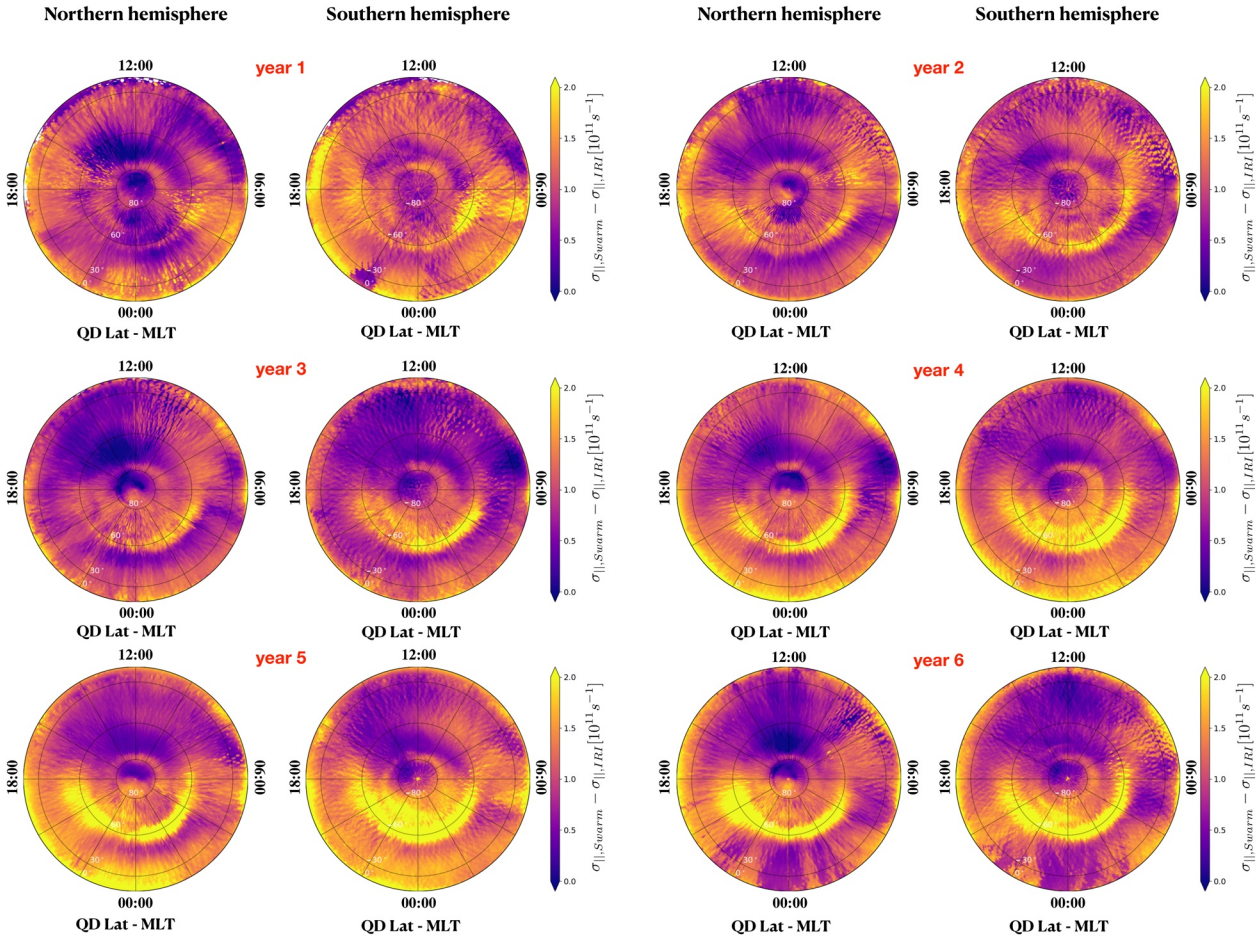

Figure 6. Yearly variation of the quantity ($\sigma_{\parallel,Swarm} - \sigma_{\parallel,IRI}$) with solar activity, i.e., starting from April 1, 2014 and up to March 31, 2020 (see Figure 2) for both the Northern and the Southern hemispheres. Maps are saturated below 0 and above 2×10^{11} s^{-1}.

Figure 7 shows $\sigma_{\parallel,Swarm} - \sigma_{\parallel,IRI}$ during quiet (AE < 50 nT) and disturbed (AE > 150 nT) geomagnetic activity levels for both the Northern (on the left) and Southern (on the right) hemispheres. Similarly to Figure 6, the most striking feature shown in Figure 7 is, again, the enhancement in the nightside in both hemispheres around ∼60° of QD latitude. This feature increases and expands equatorward of a few degrees passing from geomagnetically quiet (AE < 50 nT) to disturbed (AE > 150 nT) conditions. This enhancement not modeled by IRI is well visible even for geomagnetically quiet conditions, implying the existence of persistent features of enhanced T_e at the transition between region R2 and the edge of the middle latitude trough. Our interpretation is that in this region there is an enhancement of T_e due to both particle precipitation from the magnetosphere (e.g., from the tail regions and/or from the plasmasphere, where electrons heated by collisions with ions are diffused along the geomagnetic field lines), and the lack of a cooling mechanism such as the collisional cooling associated with the edge of the electron depletion in the nightside at middle latitudes. An increase with geomagnetic activity is also observed in correspondence with the auroral regions (where precipitations associated with R1 and R2 regions occur) and in the dayside cusp (where direct precipitations from the dayside (open) magnetosphere occur). Also, in this case, as expected, these enhancements increase in spatial extent and strength with increasing geomagnetic activity. Figure 7 confirms the nature of $\sigma_{\parallel}$ in the auroral regions, where particle precipitation is effective in connecting the magnetosphere with the ionosphere and feeding the latter of energy.

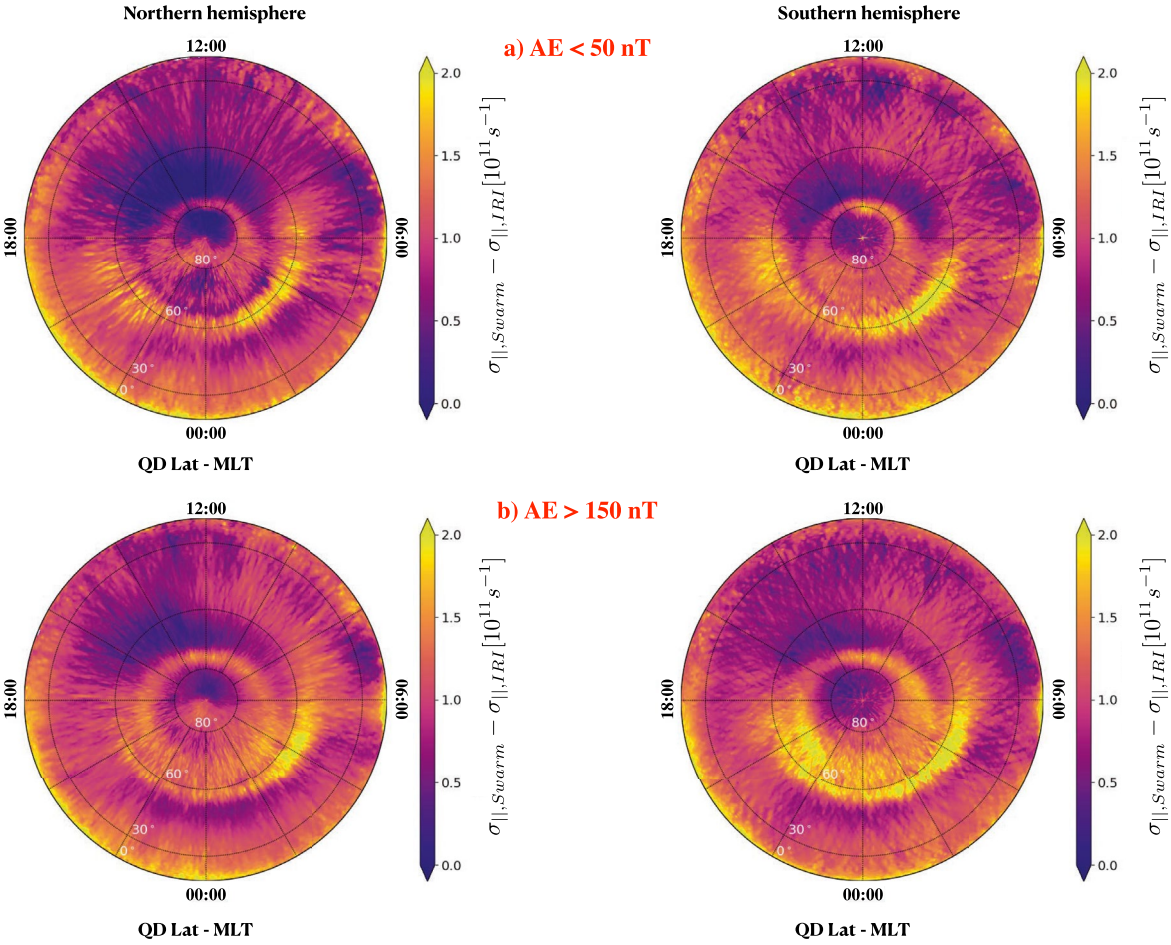

Figure 7. $(\sigma_{\parallel,Swarm} - \sigma_{\parallel,IRI})$ during quiet (AE < 50 nT) and disturbed (AE > 150 nT) geomagnetic activity for both the Northern (on the left) and Southern (on the right) hemispheres. Maps are saturated below 0 and above 2×10^{11} s^{-1}. AE, Auroral Electrojet.

4. Summary and Conclusions

We extended the work presented in Paper I by investigating the dependence of the parallel electrical conductivity, $\sigma_\parallel$, on solar and geomagnetic activity. To this aim, we took advantage of Swarm A observations at 1 s cadence from April 1, 2014 to March 31, 2020, in order to sample more than a half solar cycle from nearby solar maximum to minimum. The main results of the study are:

- Concerning the climatological behavior of $\sigma_\parallel$, we confirmed and extended the results recently obtained in Paper I by using an unprecedented long data set (6 years at 1 Hz) acquired at ~460 km of altitude, and pointed out the regions in the ionospheric F layer where $\sigma_\parallel$ is enhanced in response to complex dynamics affecting the solar wind-magnetosphere-ionosphere interaction. We confirmed the presence of peaks of $\sigma_\parallel$ in the cusp region, in the nightside auroral and subauroral regions, and in correspondence with the morning overshoot. The features associated with both diurnal and hemispheric asymmetries are also confirmed and mainly due to different sunlit conditions (diurnal and seasonal, respectively).
- There is a clear correlation between $\sigma_\parallel$ and solar activity as measured by F10.7. On the dayside, the correlation is positive, while in the nightside the correlation becomes negative. Concerning the latter, this may be due to the joint action of permanent magnetosphere-ionosphere interactions (precipitation) taking place in the auroral nightside with the decrease of n_e and anticorrelation with T_e at the edge of the main ionospheric trough.
- Both nightside and dayside features of $\sigma_\parallel$ increase and expand with geomagnetic activity, especially in the regions typically associated with R1 and R2 and at QD latitudes $\lesssim$60°. While the former regions are

associated with an increase in n_e, the latter regions are associated with a decrease of the same quantity. In light of this, we suggest that the features in the nightside around ~60° of QD latitude could originate from the transition among a regime (at higher latitudes) associated with pure particle precipitation from the magnetosphere and a regime (at lower latitudes) where the contribution from precipitations is flanked by the depletion in the edge of the main trough and the consequent reduction of collisional cooling (which, then, does not balance the enhancement of T_e).

- We estimated the contribution of particle precipitation to the variation of $\sigma_\parallel$ with solar and geomagnetic activity. This was obtained by subtracting electrical conductivity values modeled by IRI from corresponding ones computed through Swarm observations. IRI describes the main climatological variations associated with the ionospheric parameters variation. However, specific small-scale phenomena like those associated to particles precipitation and the ionospheric trough at high latitudes are not properly addressed by IRI. The results confirmed that the enhancement of $\sigma_\parallel$ during different levels of both solar and geomagnetic activity is mainly due to particle precipitation taking place in the auroral and cusp regions and at the edge of the plasmasphere, whose ionospheric signature is represented by the trough.

Of course, it is not trivial to separate all the contributions playing a role in the variation of $\sigma_\parallel$, such as different sunlit conditions (above all seasonal effects), different levels of solar and geomagnetic activity, different magnetospheric configurations, and so on. In fact, being the magnetosphere-ionosphere system is a complex one, nonlinear effects mix these contributions in a complicated way and over a wide range of scales. For this reason, despite the significant wealth in the quantity and quality of data nowadays available from different facilities, much effort is still needed to decipher the dynamics of the ionosphere in response to the Sun-Earth interaction. In this framework, we believe that this work may offer a good starting point for future works aimed at modeling (and thus forecasting) the complex dynamics in the ionospheric F layer.

Data Availability Statement

The IRI team is acknowledged for developing and maintaining the IRI model and for giving access to the corresponding Fortran code via the IRI website (http://irimodel.org/).

Acknowledgments
The results presented rely on data collected by one of the three satellites of the Swarm constellation. We thank the European Space Agency (ESA) that supports the Swarm mission. Swarm data can be accessed at http://earth.esa.int/swarm. The authors acknowledge financial support from Progetto INGV Pianeta Dinamico (codice CUP D53J19000170001) finanziato dal MIUR ("Fondo finalizzato al rilancio degli investimenti delle amministrazioni centrali dello Stato e allo sviluppo del Paese", legge 145/2018)-Task A1-2021. Part of this work is supported by the Italian MIUR-PRIN Grant 2017APKP7T on *Circumterrestrial Environment: Impact of Sun-Earth Interaction*.

References

Afonin, V. V., Bassolo, V. S., Smilauer, J., & Lemaire, J. F. (1997). Motion and erosion of the nightside plasmapause region and of the associated subauroral electron temperature enhancement: Cosmos 900 observations. *Journal of Geophysical Research*, *102*(A2), 2093–2103. https://doi.org/10.1029/96JA02497

Aggarwal, K., Nath, N., & Setty, C. (1979). Collision frequency and transport properties of electrons in the ionosphere. *Planetary and Space Science*, *27*(6), 753–768. https://doi.org/10.1016/0032-0633(79)90004-7

Amm, O. (1997). Ionospheric elementary current systems in spherical coordinates and their application. *Journal of Geomagnetism and Geoelectricity*, *49*(7), 947–955. https://doi.org/10.5636/jgg.49.947

Amm, O., Vanhamäki, H., Kauristie, K., Stolle, C., Christiansen, F., Haagmans, R., et al. (2015). A method to derive maps of ionospheric conductances, currents, and convection from the swarm multisatellite mission. *Journal of Geophysical Research: Space Physics*, *120*, 3263–3282. https://doi.org/10.1002/2014JA020154

Appleton, E. V. (1946). Two anomalies in the ionosphere. *Nature*, *157*(3995), 691. https://doi.org/10.1038/157691a0

Bilitza, D. (2018). IRI the international standard for the ionosphere. *Advances in Radio Science*, *16*, 1–11. https://doi.org/10.5194/ars-16-1-2018

Bilitza, D., Altadill, D., Truhlik, V., Shubin, V., Galkin, I., Reinisch, B., & Huang, X. (2017). International reference ionosphere 2016: From ionospheric climate to real-time weather predictions. *Space Weather*, *15*, 418–429. https://doi.org/10.1002/2016SW001593

Bilitza, D., Truhlik, V., Richards, P., Abe, T., & Triskova, L. (2007). Solar cycle variations of mid-latitude electron density and temperature: Satellite measurements and model calculations. *Advances in Space Research*, *39*(5), 779–789. https://doi.org/10.1016/j.asr.2006.11.022

Boström, R. (1964). A model of the auroral electrojets. *Journal of Geophysical Research*, *69*(23), 4983–4999. https://doi.org/10.1029/JZ069i023p04983

Boteler, D. H., & Pirjola, R. J. (2017). Modeling geomagnetically induced currents. *Space Weather*, *15*, 258–276. https://doi.org/10.1002/2016SW001499

Boteler, D. H., Pirjola, R. J., & Nevanlinna, H. (1998). The effects of geomagnetic disturbances on electrical systems at the earth's surface. *Advances in Space Research*, *22*(1), 17–27. https://doi.org/10.1016/S0273-1177(97)01096-X

Brace, L. H. (1990). Solar cycle variations in F-region Te in the vicinity of the midlatitude trough based on AE-C measurements at solar minimum and DE-2 measurements at solar maximum. *Advances in Space Research*, *10*(11), 83–88. https://doi.org/10.1016/0273-1177(90)90310-V

Brace, L. H., Chappell, C. R., Chandler, M. O., Comfort, R. H., Horwitz, J. L., & Hoegy, W. R. (1988). F region electron temperature signatures of the plasmapause based on Dynamics Explorer 1 and 2 measurements. *Journal of Geophysical Research*, *93*(A3), 1896–1908. https://doi.org/10.1029/JA093iA03p01896

Brace, L. H., Theis, R., & W. R., H. (1982). A global view of F-region electron density and temperature at solar maximum. *Geophysical Research Letters*, *9*(9), 989–992. https://doi.org/10.1029/GL009i009p00989

Brekke, A., & Hall, C. (1988). Auroral ionospheric quiet summer time conductances. *Annales Geophysicae*, *6*, 361–375.
Brinton, H. C., Grebowsky, J. M., & Brace, L. H. (1978). The high-latitude winter F region at 300 km: Thermal plasma observations from AE-C. *Journal of Geophysical Research*, *83*(A10), 4767–4776. https://doi.org/10.1029/JA083iA10p04767
Chamua, M., Bhuyan, P. K., Subrahmanyam, P., & Garg, S. C. (2007). Diurnal, seasonal, latitudinal and solar cycle variation of electron temperature in the topside F-region of the Indian zone ionosphere. *Annales Geophysicae*, *25*(9), 1995–2006. https://doi.org/10.5194/angeo-25-1995-2007
Cnossen, I., & Förster, M. (2016). North-south asymmetries in the polar thermosphere-ionosphere system: Solar cycle and seasonal influences. *Journal of Geophysical Research: Space Physics*, *121*, 612–627. https://doi.org/10.1002/2015JA021750
Coïsson, P., Nava, B., & Radicella, S. M. (2009). On the use of NeQuick topside option in IRI-2007. *Advances in Space Research*, *43*(11), 1688–1693. https://doi.org/10.1016/j.asr.2008.10.035
Cole, K. (1967). A new facet of the heating of ambient electrons by energetic charged particle streams. *Planetary and Space Science*, *15*(5), 873–879. https://doi.org/10.1016/0032-0633(67)90121-3
Cravens, T. E. (1997). *Physics of solar system plasmas*. Thomas E. Cravens.
Davis, T. N., & Sugiura, M. (1966). Auroral electrojet activity index AE and its universal time variations. *Journal of Geophysical Research*, *71*(3), 785–801. https://doi.org/10.1029/JZ071i003p00785
de la Beaujardiere, O., Alcayde, D., Fontanari, J., & Leger, C. (1991). Seasonal dependence of high-latitude electric fields. *Journal of Geophysical Research*, *96*(A4), 5723–5735. https://doi.org/10.1029/90JA01987
Duncan, R. (1960). The equatorial f-region of the ionosphere. *Journal of Atmospheric and Terrestrial Physics*, *18*(2), 89–100. https://doi.org/10.1016/0021-9169(60)90081-7
Emmert, J. T., Richmond, A. D., & Drob, D. P. (2010). A computationally compact representation of magnetic-apex and quasi-dipole coordinates with smooth base vectors. *Journal of Geophysical Research*, *115*, A08322. https://doi.org/10.1029/2010JA015326
Evans, J. V. (1970). F-region heating observed during the main phase of magnetic storms. *Journal of Geophysical Research*, *75*(25), 4815–4823. https://doi.org/10.1029/JA075i025p04815
Fok, M.-C., Kozyra, J. U., Warren, M. F., & Brace, L. H. (1991). Seasonal variations in the subauroral electron temperature enhancement. *Journal of Geophysical Research*, *96*(A6), 9773–9780. https://doi.org/10.1029/91JA00791
Föpl, H., Haerendel, G., Haser, L., Lüst, R., Melzner, F., Meyer, B., et al. (1968). Preliminary results of electric field measurements in the auroral zone. *Journal of Geophysical Research*, *73*(1), 21–26. https://doi.org/10.1029/JA073i001p00021
Foster, J. C. (1983). An empirical electric field model derived from Chatanika radar data. *Journal of Geophysical Research*, *88*(A2), 981–987. https://doi.org/10.1029/JA088iA02p00981
Friis-Christensen, E., Lühr, H., & Hulot, G. (2006). Swarm: A constellation to study the earth's magnetic field. *Earth, Planets and Space*, *58*, 351–358. https://doi.org/10.1186/BF03351933
Fuller-Rowell, T. J., & Evans, D. S. (1987). Height-integrated Pedersen and Hall conductivity patterns inferred from the TIROS-NOAA satellite data. *Journal of Geophysical Research*, *92*(A7), 7606–7618. https://doi.org/10.1029/JA092iA07p07606
Germany, G. A., Torr, D. G., Richards, P. G., Torr, M. R., & John, S. (1994). Determination of ionospheric conductivities from FUV auroral emissions. *Journal of Geophysical Research*, *99*(A12), 23297–23305. https://doi.org/10.1029/94JA02038
Giannattasio, F., De Michelis, P., Pignalberi, A., Coco, I., Consolini, G., Pezzopane, M., & Tozzi, R. (2021). Parallel electrical conductivity in the topside ionosphere derived from swarm measurements. *Journal of Geophysical Research: Space Physics*, *126*, e2020JA028452. https://doi.org/10.1029/2020JA028452
Gjerloev, J. W. (2009). A global ground-based magnetometer initiative. *Eos, Transactions American Geophysical Union*, *90*, 230–231. https://doi.org/10.1029/2009EO270002
Gololobov, A., & Golikov, I. (2019). Investigating seasonal features of electron temperature enhancement regions in the subauroral ionosphere. *Solnechno-Zemnaya Fizika*, *5*, 82–89. https://doi.org/10.12737/szf-51201909
Holzworth, R. H., Kelley, M. C., Siefring, C. L., Hale, L. C., & Mitchell, J. D. (1985). Electrical measurements in the atmosphere and the ionosphere over an active thunderstorm: 2. Direct current electric fields and conductivity. *Journal of Geophysical Research*, *90*(A10), 9824–9830. https://doi.org/10.1029/JA090iA10p09824
Iijima, T., & Potemra, T. A. (1978). Large-scale characteristics of field-aligned currents associated with substorms. *Journal of Geophysical Research*, *83*(A2), 599–615. https://doi.org/10.1029/JA083iA02p00599
Kamide, Y., & Baumjohann, W. (1993). Magnetosphere-ionosphere coupling (Vol. 23). Springer-Verlag. https://doi.org/10.1007/978-3-642-50062-6
Kamide, Y., Richmond, A. D., & Matsushita, S. (1981). Estimation of ionospheric electric fields, ionospheric currents, and field-aligned currents from ground magnetic records. *Journal of Geophysical Research*, *86*(A2), 801–813. https://doi.org/10.1029/JA086iA02p00801
Kelley, M. (2009). *The earth's ionosphere: Plasma physics and electrodynamics*. Elsevier Science.
Kirkwood, S., Opgenoorth, H., & Murphree, J. (1988). Ionospheric conductivities, electric fields and currents associated with auroral substorms measured by the EISCAT radar. *Planetary and Space Science*, *36*(12), 1359–1380. https://doi.org/10.1016/0032-0633(88)90005-0
Knudsen, D. J., Burchill, J. K., Buchert, S. C., Eriksson, A. I., Gill, R., Wahlund, J.-E., et al. (2017). Thermal ion imagers and Langmuir probes in the swarm electric field instruments. *Journal of Geophysical Research: Space Physics*, *122*, 2655–2673. https://doi.org/10.1002/2016JA022571
Kofman, W., & Wickwar, V. B. (1984). Very high electron temperatures in the daytime f region at sondrestrom. *Geophysical Research Letters*, *11*(9), 919–922. https://doi.org/10.1029/GL011i009p00919
Kozyra, J. U., Brace, L. H., Cravens, T. E., & Nagy, A. F. (1986). A statistical study of the subauroral electron temperature enhancement using Dynamics Explorer 2 Langmuir probe observations. *Journal of Geophysical Research*, *91*(A10), 11270–11280. https://doi.org/10.1029/JA091iA10p11270
Laundal, K. M., & Richmond, A. D. (2017). Magnetic coordinate systems. *Space Science Reviews*, *1*, 27–59. https://doi.org/10.1007/s11214-016-0275-y
Liu, H., & Lühr, H. (2005). Strong disturbance of the upper thermospheric density due to magnetic storms: Champ observations. *Journal of Geophysical Research*, *110*, A09S29. https://doi.org/10.1029/2004JA010908
Lomidze, L., Knudsen, D. J., Burchill, J., Kouznetsov, A., & Buchert, S. C. (2018). Calibration and validation of swarm plasma densities and electron temperatures using ground-based radars and satellite radio occultation measurements. *Radio Science*, *53*, 15–36. https://doi.org/10.1002/2017RS006415
Marklund, G., Sandahl, I., & Opgenoorth, H. (1982). A study of the dynamics of a discrete auroral arc. *Planetary and Space Science*, *30*(2), 179–197. https://doi.org/10.1016/0032-0633(82)90088-5

McDonald, J., & Williams, P. (1980). The relationship between ionospheric temperature, electron density and solar activity. *Journal of Atmospheric and Terrestrial Physics*, *42*(1), 41–44. https://doi.org/10.1016/0021-9169(80)90121-X
Medvedeva, I. V., & Ratovsky, K. G. (2019). Solar activity influence on the mesopause temperature and F2 peak electron density. In *2019 photonics electromagnetics research symposium-spring (PIERS-Spring)* (pp. 3958–3964). https://doi.org/10.1109/PIERS-Spring46901.2019.9017812
Mende, S. B., Eather, R. H., Rees, M. H., Vondrak, R. R., & Robinson, R. M. (1984). Optical mapping of ionospheric conductance. *Journal of Geophysical Research*, *89*(A3), 1755–1763. https://doi.org/10.1029/JA089iA03p01755
Milan, S., Clausen, L., Coxon, J., Carter, J., Walach, M.-T., Laundal, K. M., et al. (2017). Overview of solar wind–magnetosphere–ionosphere–atmosphere coupling and the generation of magnetospheric currents. *Space Science Reviews*, *206*, 547–573. https://doi.org/10.1007/s11214-017-0333-0
Mitra, S. K. (1946). Geomagnetic control of region F2 of the ionosphere. *Nature*, *158*(4019), 668–669. https://doi.org/10.1038/158668a0
Moen, J., & Brekke, A. (1990). On the importance of ion composition to conductivities in the auroral ionosphere. *Journal of Geophysical Research*, *95*(A7), 10687–10693. https://doi.org/10.1029/JA095iA07p10687
Moen, J., & Brekke, A. (1993). The solar flux influence on quiet time conductances in the auroral ionosphere. *Geophysical Research Letters*, *20*(10), 971–974. https://doi.org/10.1029/92GL02109
Moldwin, M. (2008). *An introduction to space weather*. Cambridge University Press. https://doi.org/10.1017/CBO9780511801365
Mozer, F. S., & Serlin, R. (1969). Magnetospheric electric field measurements with balloons. *Journal of Geophysical Research*, *74*(19), 4739–4754. https://doi.org/10.1029/JA074i019p04739
Nava, B., Coïsson, P., & Radicella, S. (2008). A new version of the NeQuick ionosphere electron density model. *Journal of Atmospheric and Solar-Terrestrial Physics*, *70*, 1856–1862. https://doi.org/10.1016/j.jastp.2008.01.015
Newell, P. T., & Gjerloev, J. W. (2011). Evaluation of SuperMAG auroral electrojet indices as indicators of substorms and auroral power. *Journal of Geophysical Research*, *116*, A12211. https://doi.org/10.1029/2011JA016779
Nicolet, M. (1953). The collision frequency of electrons in the ionosphere. *Journal of Atmospheric and Terrestrial Physics*, *3*(4), 200–211. https://doi.org/10.1016/0021-9169(53)90110-X
Nishino, M., Nozawa, S., & Holtet, J. A. (1998). Daytime ionospheric absorption features in the polar cap associated with poleward drifting f-region plasma patches. *Earth, Planets and Space*, *50*(2), 107–117. https://doi.org/10.1186/BF03352092
Pignalberi, A., Pezzopane, M., Tozzi, R., De Michelis, P., & Coco, I. (2016). Comparison between IRI and preliminary Swarm Langmuir probe measurements during the St. Patrick storm period. *Earth, Planets and Space*, *68*(1), 93. https://doi.org/10.1186/s40623-016-0466-5
Pirjola, R., Kauristie, K., Lappalainen, H., Viljanen, A., & Pulkkinen, A. (2005). Space weather risk. *Space Weather*, *3*, S02A02. https://doi.org/10.1029/2004SW000112
Poedjono, B., Beck, N., Buchanan, A., Borri, L., Maus, S., Finn, C. A., et al. (2013). *Improved geomagnetic referencing in the arctic environment*. Society of Petroleum Engineers.
Prölss, G. W. (2006a). Electron temperature enhancement beneath the magnetospheric cusp. *Journal of Geophysical Research*, *111*, A07304. https://doi.org/10.1029/2006JA011618
Prölss, G. W. (2006b). Subauroral electron temperature enhancement in the nighttime ionosphere. *Annales Geophysicae*, *24*(7), 1871–1885. https://doi.org/10.5194/angeo-24-1871-2006
Pulkkinen, A., Amm, O., & Viljanen, A. (2003). Ionospheric equivalent current distributions determined with the method of spherical elementary current systems. *Journal of Geophysical Research*, *108*(A2), 1053. https://doi.org/10.1029/2001JA005085
Rasmussen, C. E., Schunk, R. W., & Wickwar, V. B. (1988). A photochemical equilibrium model for ionospheric conductivity. *Journal of Geophysical Research*, *93*(A9), 9831–9840. https://doi.org/10.1029/JA093iA09p09831
Ratcliffe, J. (1973). An introduction to the ionosphere and magnetosphere. J. A. Ratcliffe, Cambridge University Press, 1972, pp. 256 £4. *Quarterly Journal of the Royal Meteorological Society*, *99*(419), 208–209. https://doi.org/10.1002/qj.49709941923
Reigber, C., Lühr, H., & Schwintzer, P. (2002). CHAMP mission status. *Advances in Space Research*, *30*(2), 129–134. https://doi.org/10.1016/S0273-1177(02)00276-4
Richmond, A. D. (1995). Ionospheric electrodynamics using magnetic apex coordinates. *Journal of Geomagnetism and Geoelectricity*, *47*(2), 191–212. https://doi.org/10.5636/jgg.47.191
Rishbeth, H. (1997). The ionospheric E-layer and F-layer dynamos—A tutorial review. *Journal of Atmospheric and Solar-Terrestrial Physics*, *59*(15), 1873–1880. https://doi.org/10.1016/S1364-6826(97)00005-9
Rishbeth, H., & Garriott, O. K. (1969). *Introduction to ionospheric physics*. Academic Press.
Rishbeth, H., & Müller-Wodarg, I. C. F. (1999). Vertical circulation and thermospheric composition: A modelling study. *Annales Geophysicae*, *17*(6), 794–805. https://doi.org/10.1007/s00585-999-0794-x
Robinson, R., Tsunoda, R. T., Vickrey, J. F., & Guerin, L. (1985a). Sources of F region ionization enhancements in the nighttime auroral zone. *Journal of Geophysical Research*, *90*(A8), 7533–7546. https://doi.org/10.1029/JA090iA08p07533
Robinson, R., Vondrak, R. R., & Potemra, T. A. (1985b). Auroral zone conductivities within the field-aligned current sheets. *Journal of Geophysical Research*, *90*(A10), 9688–9696. https://doi.org/10.1029/JA090iA10p09688
Savitzky, A., & Golay, M. J. E. (1964). Smoothing and differentiation of data by simplified least squares procedures. *Analytical Chemistry*, *36*(8), 1627–1639. https://doi.org/10.1021/ac60214a047
Schunk, R. W., & Nagy, A. F. (1978). Electron temperatures in the F region of the ionosphere: Theory and observations. *Reviews of Geophysics*, *16*(3), 355–399. https://doi.org/10.1029/RG016i003p00355
Sharma, D. K., Rai, J., Israil, M., Subrahmanyam, P., Chopra, P., & Garg, S. C. (2004). Enhancement in electron and ion temperatures due to solar flares as measured by SROSS-C2 satellite. *Annales Geophysicae*, *22*(6), 2047–2052. https://doi.org/10.5194/angeo-22-2047-2004
Shim, J. S., Kuznetsova, M., Rastätter, L., Bilitza, D., Butala, M., Codrescu, M., & Sutton, E. (2012). Cedar electrodynamics thermosphere ionosphere (ETI) challenge for systematic assessment of ionosphere/thermosphere models: Electron density, neutral density, Nmf2, and hmf2 using space based observations. *Space Weather*, *10*, S10004. https://doi.org/10.1029/2012SW000851
Shim, J. S., Kuznetsova, M., Rastätter, L., Hesse, M., Bilitza, D., Butala, M., & Rideout, B. (2011). Cedar electrodynamics thermosphere ionosphere (ETI) challenge for systematic assessment of ionosphere/thermosphere models: Nmf2, hmf2, and vertical drift using ground-based observations. *Space Weather*, *9*, S12003. https://doi.org/10.1029/2011SW000727
Singh, R. N. (1966). The effective electron collision frequency in the lower F region of the ionosphere. *Proceedings of the Physical Society*, *87*(2), 425–428. https://doi.org/10.1088/0370-1328/87/2/311
Spiro, R. W., Reiff, P. H., & Maher, L. J. Jr. (1982). Precipitating electron energy flux and auroral zone conductances-an empirical model. *Journal of Geophysical Research*, *87*(A10), 8215–8227. https://doi.org/10.1029/JA087iA10p08215

Stolle, C., Liu, H., Truhlík, V., Lühr, H., & Richards, P. G. (2011). Solar flux variation of the electron temperature morning overshoot in the equatorial f region. *Journal of Geophysical Research*, *116*, A04308. https://doi.org/10.1029/2010JA016235

Takeda, M. (2002). The correlation between the variation in ionospheric conductivity and that of the geomagnetic Sq field. *Journal of Atmospheric and Solar-Terrestrial Physics*, *64*(15), 1617–1621. https://doi.org/10.1016/S1364-6826(02)00140-2

Takeda, M., & Araki, T. (1985). Electric conductivity of the ionosphere and nocturnal currents. *Journal of Atmospheric and Terrestrial Physics*, *47*(6), 601–609. https://doi.org/10.1016/0021-9169(85)90043-1

Themens, D. R., Jayachandran, P. T., Galkin, I., & Hall, C. (2017). The empirical Canadian high arctic ionospheric model (E-CHAIM): Nmf2 and hmf2. *Journal of Geophysical Research: Space Physics*, *122*, 9015–9031. https://doi.org/10.1002/2017JA024398

Truhlik, V., Bilitza, D., & Triskova, L. (2012). A new global empirical model of the electron temperature with the inclusion of the solar activity variations for IRI. *Earth, Planets and Space*, *64*(6), 531–543. https://doi.org/10.5047/eps.2011.10.016

Tsagouri, I., Goncharenko, L., Shim, J. S., Belehaki, A., Buresova, D., & Kuznetsova, M. M. (2018). Assessment of current capabilities in modeling the ionospheric climatology for space weather applications: foF2 and hmF2. *Space Weather*, *16*, 1930–1945. https://doi.org/10.1029/2018SW002035

Vickrey, J. F., Vondrak, R. R., & Matthews, S. J. (1981). The diurnal and latitudinal variation of auroral zone ionospheric conductivity. *Journal of Geophysical Research*, *86*(A1), 65–75. https://doi.org/10.1029/JA086iA01p00065

Wang, H., Lühr, H., & Ma, S. Y. (2005). Solar zenith angle and merging electric field control of field-aligned currents: A statistical study of the southern hemisphere. *Journal of Geophysical Research*, *110*, A03306. https://doi.org/10.1029/2004JA010530

Wang, W., Burns, A. G., & Killeen, T. L. (2006). A numerical study of the response of ionospheric electron temperature to geomagnetic activity. *Journal of Geophysical Research*, *111*, A11301. https://doi.org/10.1029/2006JA011698

Weygand, J. M., Amm, O., Viljanen, A., Angelopoulos, V., Murr, D., Engebretson, M. J., & Mann, I. (2011). Application and validation of the spherical elementary currents systems technique for deriving ionospheric equivalent currents with the North American and Greenland ground magnetometer arrays. *Journal of Geophysical Research*, *116*, A03305. https://doi.org/10.1029/2010JA016177

Willmore, A. P. (1965). Geographical and solar activity variations in the electron temperature of the upper F-region. *Proceedings of the Royal Society of London-Series A: Mathematical and Physical Sciences*, *286*(1407), 537–558. https://doi.org/10.1098/rspa.1965.0163

Zmuda, A. J., & Armstrong, J. C. (1974). The diurnal flow pattern of field-aligned currents. *Journal of Geophysical Research*, *79*(31), 4611–4619. https://doi.org/10.1029/JA079i031p04611

Zmuda, A. J., Martin, J. H., & Heuring, F. T. (1966). Transverse magnetic disturbances at 1100 kilometers in the auroral region. *Journal of Geophysical Research*, *71*(21), 5033–5045. https://doi.org/10.1029/JZ071i021p05033